PNAS RESEARCH ARTICLE | APPLIED PHYSICAL SCIENCES

On the absence of the ultimate regime in turbulent thermal convection

Harshit Tiwari[a], Lekha Sharma[a], and Mahendra K. Verma[a,b,1]

Edited by John S. Wettlaufer, Yale University, New Haven, CT; received May 26, 2025; accepted September 29, 2025 by Editorial Board Member Christopher Jarzynski

Quantifying heat transport in turbulent convection remains a challenge. The two competing models of heat transport predict that the nondimensional heat flux, known as the Nusselt number (Nu), is proportional to $Ra^{1/3}$ (classical scaling) and $Ra^{1/2}$ (ultimate-regime scaling), where Ra is the Rayleigh number. Some experiments and simulations report that the Nusselt number transitions from near classical scaling, $Ra^{0.30}$, to a larger power law when the boundary layer turns turbulent near $Ra \approx 10^{14}$. However, others find $Ra^{0.30}$ scaling to continue for larger Ra. In this work, we perform a comparative study of Rayleigh-Bénard, compressible, and periodic convection in two and three dimensions using direct numerical simulations. We show that up to $Ra = 10^{16}$ in two dimensions and up to $Ra = 10^{13}$ in three dimensions, the positive and negative energy fluxes in Rayleigh-Bénard and compressible convection are nearly equal. However, in the distribution function, the positive fluxes have longer tails than the negative ones, and the differences between the positive and negative fluxes scale as $Ra^{-0.20}$, which leads to $Nu \sim Ra^{0.30}$. The above robust and universal properties, even in the presence of a logarithmic layer in compressible convection, indicate a likely absence of the ultimate regime in turbulent thermal convection. In contrast, periodic convection, which is related to the ultimate regime, exhibits a predominantly positive heat flux.

turbulent convection | turbulent heat transport | ultimate regime of convection | Rayleigh–Benard convection | compressible convection

Significance

Thermal convection efficiently transports heat in astrophysical and engineering flows. Normally, we expect hot plumes to ascend and cold plumes to descend, resulting in a positive heat flux. This paper presents evidence that in Rayleigh-Bénard and compressible convection, the upper boundary deflects the hot plumes downward, thereby inducing a negative flux. The difference between the positive and negative heat fluxes decreases with the Rayleigh number, yielding the classical Nu scaling. These subtle features of heat flux help solve a long-standing problem in the heat transport of turbulent convection and pave the way for significantly improved heat transport models of astrophysical, atmospheric, and engineering flows.

Turbulent convection, driven by heating from below and cooling from above, enhances heat transport compared to thermal conduction. It plays an important role in astrophysical systems, such as the atmospheres of planets and stars; in engineering systems, such as boilers and heat exchangers; and in the kitchen, such as tea kettles. Even though these systems have varying configurations and fluid properties, they exhibit certain universal properties. For example, stellar convection with plasmas is compressive, whereas thermal convection in Earth's oceans has nearly constant material density. Researchers have performed convection experiments and simulations on different fluids (air, water, plasmas, and helium gas) in Cartesian boxes and spherical shells with different aspect ratios. Yet, heat transport in turbulent convection follows certain universal features. In particular, the normalized rms velocity and the convective heat transport vary as approximately $(\Delta T)^{1/2}$ and $(\Delta T)^{1/3}$, respectively, where ΔT is the temperature difference between the hot and cold surfaces (1–6). In this paper, our focus is on the universal properties of heat transport. We demonstrate that the thermal boundaries induce negative heat flux, and the difference between the positive and negative heat fluxes leads to nearly classical $(\Delta T)^{1/3}$ scaling.

First, we discuss heat transport in a controlled setup called Rayleigh-Bénard convection (RBC) in which a fluid confined between two plates is heated from below and cooled at the top. RBC assumes Boussinesq approximation, according to which the fluid density is constant, except in the buoyancy term, and the fluid parameters are constant in space and time (1–6). The two nondimensional system parameters are the Rayleigh number (Ra), which is the ratio of the buoyancy term and the diffusive term, and the Prandtl number (Pr), which is the ratio of the kinematic viscosity and the thermal diffusivity. The heat transport in the flow is quantified using a nondimensional parameter Nusselt number (Nu), which is the ratio of total heat transfer and the conductive heat transfer. In 1954, based on the assumption that the heat flux is independent of box height, Priestley (7) derived that Nu is proportional to $Ra^{1/3}$, which is called classical scaling. In the same year, Malkus (8) arrived at a similar scaling relation by extremizing the heat transport for various temperature profiles. Using mixing length theory, in 1962,

Author affiliations: [a]Department of Physics, Indian Institute of Technology Kanpur, Kanpur 208016, India; and [b]Kotak School of Sustainability, Indian Institute of Technology Kanpur, Kanpur 208016, India

Author contributions: H.T. and M.K.V. designed research; H.T., L.S., and M.K.V. performed research; H.T., L.S., and M.K.V. contributed new reagents/analytic tools; H.T., L.S., and M.K.V. analyzed data; and H.T., L.S., and M.K.V. wrote the paper.

The authors declare no competing interest.

This article is a PNAS Direct Submission. J.S.W. is a guest editor invited by the Editorial Board.

[1]To whom correspondence may be addressed. Email: mkv@iitk.ac.in.

This article contains supporting information online at https://www.pnas.org/lookup/suppl/doi:10.1073/pnas.2513474122/-/DCSupplemental.

Published October 31, 2025.

Kraichnan (9) argued that for moderate Prandtl numbers, the boundary layer becomes turbulent at large Rayleigh numbers, leading to a scaling of Nu $\sim$ $[\mathrm{Ra}(\log \mathrm{Ra})^{-3}]^{1/2}$. The scaling Nu $\sim$ $\mathrm{Ra}^{1/2}$ is called ultimate regime scaling. Howard (10) also employed variational principles and obtained an upper bound for Nu as $\sqrt{3\mathrm{Ra}/64}$. Spiegel (11, 12) proposed that the turbulent heat flux should be independent of the molecular diffusion, which leads to Nu $\propto$ $(\mathrm{RaPr})^{1/2}$. In 1966, Howard (13) critically summarized the results of Malkus, Herring, Kraichnan, and Spiegel. In the same paper, Howard derived that Nu $\propto$ $(\mathrm{Ra})^{1/3}$ using an analytical model of diffusion and marginal stability in the turbulent boundary layer (14). See also Doering (15) for later applications of variational principles for computing upper bounds on the Nusselt number. Shraiman and Siggia (16) derived exact relations connecting Nu, Ra, and Pr, while Grossmann and Lohse (17) developed a phenomenological framework that predicts Nu scaling based on bulk and boundary-layer dissipation. See Doering (18) for a concise historical perspective.

The existence of an ultimate regime remains a central question in the field, leading to extensive experimental and numerical investigations. Up to Ra $\sim$ 10^{12}, most data are consistent with the classical scaling exponent $\approx$ 1/3 (1–3, 5, 17). For Ra beyond 10^{14}, using experiments and numerical simulations, Chavanne et al. (19), He et al. (20), and Zhu et al. (21) show that the Nu scaling exponent increases gradually up to 0.38 near Ra = 10^{15}; it is assumed that the exponent will reach 1/2 asymptotically (22, 23). However, the experimental results of Niemela et al. (24), Niemela and Sreenivasan (25), and Urban et al. (26), and the numerical simulations of Iyer et al. (27) indicate Nu $\sim$ $\mathrm{Ra}^{0.30}$ up to Ra = 10^{16}. Interestingly, RBC with free-slip boundary condition exhibits approximately 1/3 scaling, even though such flows are turbulent everywhere without a viscous boundary layer (28, 29). Hence, the connection between the ultimate regime and the turbulent boundary layer needs a closer examination, as articulated in a recent article by Doering (18).

The Boussinesq approximation does not hold in systems exhibiting strong density fluctuations, e.g., solar convection (4). Convection in such systems, referred to as compressible convection (CC), has been simulated by John and Schumacher (30, 31) and Tiwari et al. (32) up to Ra $\approx$ 10^{15} in two dimensions (2D) and up to Ra $\approx$ 10^{11} in three dimensions (3D). These authors report that Nu $\sim$ $\mathrm{Ra}^{0.30}$. In this paper, we extend this scaling up to Ra of 10^{16} in 2D and up to 10^{13} in 3D. We also demonstrate that a logarithmic layer is present in the viscous and thermal boundary layers of 2D compressible convection. However, the nature of the boundary layers in 3D compressible convection is uncertain. Periodic convection (PC) is another class of thermal convection, in which a fluid within a periodic box (one without walls) is subjected to a vertical temperature gradient. Lohse and Toschi (33), Verma et al. (28), and Winchester et al. (34) simulated periodic convection and reported that Nu $\sim$ $\mathrm{Ra}^{1/2}$, which aligns with the scaling of the ultimate regime.

This paper derives important insights by examining the Nusselt number scaling in a combined study of periodic, compressible, and Rayleigh-Bénard convection. While the bulk flows are turbulent at large Ra in both no-slip and free-slip versions of RBC and compressible convection, some of these systems exhibit logarithmic layers, but others do not. Still, all of them show near classical 1/3 scaling. In this paper, we compute the local heat flux $u_z(\mathbf{r})\,T(\mathbf{r})$, where u_z, T are the vertical velocity and temperature, respectively. Surprisingly, the heat flux takes both positive and negative values with nearly equal probabilities, but the positive flux has a longer tail in the distribution function. The positive heat flux is natural, with hot plumes ascending and cold plumes descending, but the negative flux arises due to the thermal plates. For example, a downward deflection of the hot plumes by the top plate yields negative flux. The difference between the positive and negative heat fluxes scales as $\mathrm{Ra}^{-0.20}$, which results in a correction to the Nu $\sim$ $\mathrm{Ra}^{1/2}$ scaling, yielding Nu $\sim$ $\mathrm{Ra}^{1/2-0.20}$ or Nu $\sim$ $\mathrm{Ra}^{0.30}$. Interestingly, the negative heat flux is absent in periodic convection that leads to Nu $\sim$ $\mathrm{Ra}^{1/2}$. Hence, the influence of thermal plates on the bulk flow leads to Nu $\sim$ $\mathrm{Ra}^{0.30}$ scaling, with the boundary layers appearing to play a marginal role in this phenomenon.

The structure of the paper is as follows. We take numerical data of RBC, compressible convection, and periodic convection and analyze the local heat flux and its probability distribution; the above quantities provide valuable insights into the Nu scaling. We also examine the boundary layers of compressible convection. A collective view of these systems reveals a likely absence of the ultimate regime in turbulent convection.

Results

We present all our results in this section. We start with the system and data description.

Systems and Datasets Employed. Here, we provide a brief description of the datasets used in this paper. We generate datasets for PC and CC using direct numerical simulations. However, RBC simulation datasets have been borrowed from Bhattacharya et al. (35) for 3D simulations and from Samuel and Verma (36) and Samuel (37) for 2D simulations. The details of the equations and numerical methods employed can be found in *Materials and Methods*. For the three cases (PC, RBC, CC), the Prandtl number is defined as $\mathrm{Pr} = \nu/\kappa$, whereas for RBC and PC, the Rayleigh number is defined as $\mathrm{Ra} = \alpha(\Delta T)gd^3/(\nu\kappa)$, where ν, κ, α are, respectively, the kinematic viscosity, thermal diffusivity, and the thermal expansion coefficient of the fluid, g is the acceleration due to gravity, and ΔT is the temperature difference between the thermal plates that are separated by distance d. The definition of the Rayleigh number for compressible convection differs slightly (38). The parameters specific to compressible convection are superadiabaticity (ϵ), which is the excess temperature gradient relative to the adiabatic profile, and dissipation number (D), which is the nondimensional adiabatic temperature drop. See *Materials and Methods*, Spiegel (38), Graham (39), and Schumacher and Sreenivasan (4) for the definitions of these parameters.

Periodic convection (28, 33) was simulated using a spectral code Tarang-py (40) in a $(2\pi)^2$ domain with grid points ranging from 64^2 to 1024^2, and in a $(2\pi)^3$ domain with grid points ranging from 128^3 to 256^3. The range of Ra is 10^4 to 10^8 in 2D and 10^4 to 10^7 in 3D. The Prandtl number is 1 for all the runs. In Table 1, we list the Reynolds number based on the box size ($\mathrm{Re} = UL/\nu$), the Nusselt number (Nu), the magnitudes of the average positive and negative fluxes $|\langle F_{z\pm}\rangle|$ (to be discussed below), and the resolution parameter ($\mathcal{R}_\eta = \min_i(\eta/\Delta x_i)$). In the above formulas, U, L, and ν are the rms velocity, box size, and nondimensional kinematic viscosity ($\sqrt{\mathrm{Pr}/\mathrm{Ra}}$), respectively; η is the Kolmogorov length; and Δx_i is the grid spacing in the i-th direction (41, 42). The Reynolds and Nusselt numbers for these flows are sufficiently large.

Table 1. Simulation parameters for periodic convection (P2D, P3D), RBC (R2D, R3D), and compressible convection (C2D, C3D), with 2D and 3D representing space dimensions: Rayleigh number Ra, Prandtl number Pr, grid size, aspect ratio Γ, Reynolds number Re, Nusselt number Nu, absolute values of mean positive and negative vertical heat fluxes ($|\langle F_{z+}\rangle|$, $|\langle F_{z-}\rangle|$), the von Kármán constants for the viscous and thermal boundary layers (κ_u, κ_T), and resolution parameter $\mathcal{R}_\eta$

Run	System	Ra	Pr	Grid size	Γ	Re	Nu	$\lvert\langle F_{z+}\rangle\rvert$	$\lvert\langle F_{z-}\rangle\rvert$	κ_u	κ_T	$\mathcal{R}_\eta$
1	P2D	10^4	1	64^2	1	$(9.64 \pm 0.25) \times 10^2$	92 ± 14	1.94	0.55	NA	NA	1.08
2	P2D	10^5	1	128^2	1	$(3.42 \pm 0.02) \times 10^3$	229 ± 37	2.56	0.72	NA	NA	1.23
3	P2D	10^6	1	256^2	1	$(1.05 \pm 0.03) \times 10^4$	801 ± 143	2.49	0.80	NA	NA	1.44
4	P2D	10^7	1	512^2	1	$(2.61 \pm 0.01) \times 10^4$	$2{,}103 \pm 550$	2.37	0.94	NA	NA	1.58
5	P2D	10^8	1	$1{,}024^2$	1	$(1.27 \pm 0.003) \times 10^5$	$9{,}430 \pm 2{,}500$	2.65	0.79	NA	NA	1.71
6	P3D	10^4	1	128^3	1	$(1.12 \pm 0.003) \times 10^3$	95 ± 14	1.76	0.20	NA	NA	1.11
7	P3D	10^5	1	128^3	1	$(2.99 \pm 0.02) \times 10^3$	231 ± 37	1.50	0.19	NA	NA	1.30
8	P3D	10^6	1	180^3	1	$(9.52 \pm 0.04) \times 10^3$	807 ± 68	1.48	0.21	NA	NA	1.04
9	P3D	10^7	1	256^3	1	$(2.98 \pm 0.002) \times 10^4$	$2{,}223 \pm 231$	1.38	0.20	NA	NA	1.03
10	R2D	10^9	1	$1{,}024 \times 512$	2	$(1.47 \pm 0.028) \times 10^4$	48 ± 14	0.101	0.09	-	-	1.21
11	R2D	10^{10}	1	$2{,}048 \times 1{,}024$	2	$(5.05 \pm 0.36) \times 10^4$	94 ± 29	0.108	0.102	-	-	1.24
12	R2D	10^{11}	1	$4{,}096 \times 2{,}048$	2	$(1.97 \pm 0.08) \times 10^5$	190 ± 12	0.114	0.11	-	-	1.26
13	R2D	10^{12}	1	$8{,}192 \times 4{,}096$	2	$(4.58 \pm 0.1) \times 10^5$	356 ± 17	0.099	0.098	-	-	1.14
14	R2D	10^{13}	1	$1{,}6384 \times 8{,}192$	2	$(1.16 \pm 0.02) \times 10^6$	677 ± 39	0.082	0.080	-	-	1.08
15	R2D	10^{14}	1	$12{,}288^2$	1	$(3.44 \pm 0.007) \times 10^6$	$1{,}280 \pm 130$	0.068	0.066	-	-	1.06
16	R2D	10^{15}	1	$16{,}384^2$	1	$(1.08 \pm 0.001) \times 10^7$	$2{,}875 \pm 225$	0.075	0.073	-	-	1.07
17	R2D	10^{16}	1	$32{,}768^2$	1	$(3.42 \pm 0.004) \times 10^7$	$5{,}680 \pm 380$	0.085	0.082	-	-	1.05
18	R3D	10^6	1	257^3	1	$(1.47 \pm 0.08) \times 10^2$	8.2 ± 0.9	0.056	0.041	-	-	4.92
19	R3D	10^7	1	257^3	1	$(4.91 \pm 0.14) \times 10^2$	16.3 ± 1.3	0.048	0.037	-	-	2.31
20	R3D	10^8	1	513^3	1	$(1.53 \pm 0.049) \times 10^3$	31.4 ± 2.9	0.044	0.038	-	-	2.19
21	R3D	10^9	1	$1{,}025^3$	1	$(4.7 \pm 0.092) \times 10^3$	61.2 ± 4.2	0.043	0.034	-	-	2.06
22	C2D	10^9	0.7	513^2	1	$(1.3 \pm 0.1) \times 10^4$	22 ± 2	0.026	0.019	0.93	3.7	0.82
23	C2D	10^{10}	0.7	$1{,}025^2$	1	$(4.4 \pm 0.2) \times 10^4$	46 ± 3	0.027	0.023	0.87	3.6	0.66
24	C2D	10^{11}	0.7	$2{,}049^2$	1	$(1.38 \pm 0.08) \times 10^5$	103 ± 12	0.028	0.025	0.83	3.9	0.57
25	C2D	10^{12}	0.7	$4{,}097^2$	1	$(4.7 \pm 0.2) \times 10^5$	238 ± 23	0.036	0.033	0.78	5.1	0.57
26	C2D	10^{13}	0.7	$8{,}193^2$	1	$(1.46 \pm 0.02) \times 10^6$	489 ± 35	0.036	0.035	0.69	8.6	0.56
27	C2D	10^{14}	0.7	$12{,}001^2$	0.8	$(4.04 \pm 0.05) \times 10^6$	909 ± 112	0.034	0.032	0.68	9.9	0.51
28	C2D	10^{15}	0.7	$16{,}385^2$	0.8	$(1.24 \pm 0.02) \times 10^7$	$2{,}204 \pm 220$	0.031	0.030	0.60	10	0.52
29	C2D	10^{16}	0.7	$24{,}001^2$	0.8	$(4.1 \pm 0.1) \times 10^7$	$3{,}893 \pm 510$	0.028	0.027	0.47	11	0.51
30	C3D	10^7	0.7	$33^2 \times 129$	0.25	$(3.6 \pm 0.5) \times 10^2$	5 ± 1	0.0095	0.0051	-	-	0.76
31	C3D	10^8	0.7	$65^2 \times 257$	0.25	$(1.5 \pm 0.1) \times 10^3$	14 ± 1	0.012	0.0072	-	8.8	0.76
32	C3D	10^9	0.7	$129^2 \times 513$	0.25	$(4.3 \pm 0.3) \times 10^3$	28 ± 2	0.0095	0.0063	-	10	0.72
33	C3D	10^9	0.7	513^3	1	$(6.0 \pm 0.1) \times 10^3$	27.5 ± 0.7	0.011	0.0075	-	7.1	0.72
34	C3D	10^{10}	0.7	$257^2 \times 1{,}025$	0.25	$(1.22 \pm 0.08) \times 10^4$	55 ± 3	0.0073	0.0055	-	13	0.69
35	C3D	10^{11}	0.7	$513^2 \times 2{,}049$	0.25	$(3.82 \pm 0.06) \times 10^4$	112 ± 4	0.0062	0.0046	-	16	0.66
36	C3D	10^{12}	0.7	$451^2 \times 3{,}601$	0.125	$(7.86 \pm 0.22) \times 10^4$	202 ± 34	0.0051	0.0042	-	19	0.59
37	C3D	10^{13}	0.7	$501^2 \times 5{,}001$	0.125	$(2.43 \pm 0.09) \times 10^5$	412 ± 56	0.0034	0.0025	-	24	0.55

Compressible convection was simulated using the finite-difference code Dhara (32) with grid points ranging from 513^2 to $24{,}001^2$ for 2D flows and with grid points ranging from $33^2 \times 129$ to $512^2 \times 5{,}001$ for 3D flows. We chose Ra ranging from 10^9 to 10^{16} in 2D and Ra ranging from 10^7 to 10^{13} in 3D. The aspect ratio Γ varies from 1 to 0.125 (Table 1). We chose Pr = 0.7, superadiabaticity $\epsilon = 0.1$, dissipation number $D = 0.5$, and the ratio of specific heat capacities $\gamma = 1.3$. The Reynolds number ranges from 360 to 4×10^7. Table 1 lists Ra, Pr, Re, Nu, $|\langle F_{z\pm}\rangle|$, $\mathcal{R}_\eta$, and von Kármán constants for viscous and thermal boundary layers, κ_u, κ_T, respectively, which will be discussed later.

RBC simulations were performed using the finite-difference Boussinesq code SARAS (43). All runs have Pr = 1. The Rayleigh number ranges from 10^9 to 10^{16} in 2D and from 10^6 to 10^9 in 3D. For 2D, the aspect ratio $\Gamma = 2$ up to $\mathrm{Ra} = 10^{13}$, after which Γ is unity. However, $\Gamma = 1$ for all 3D runs. The values of Re, Nu, $|\langle F_{z\pm}\rangle|$, and $\mathcal{R}_\eta$ for these runs are listed in Table 1.

Our simulations are well resolved, both in the bulk and in the boundary layers. In addition, our simulations have converged to steady states (see *Materials and Methods* and *SI Appendix* for details on numerical resolution and convergence). Next, we describe the properties of the boundary layers in turbulent convection.

Boundary Layers in Turbulent Convection. In a flow past a flat plate, the appearance of a logarithmic layer in the boundary layer signals transition to turbulence (44). Inspired by this observation,

researchers have examined the boundary layers in turbulent RBC using experiments and simulations. For large Ra, Ahlers et al. (45) and He et al. (20) reported a logarithmic layer in their convection experiments with sulfur hexafluoride (SF_6). Zhu et al. (21) simulated 2D turbulent convection and reported a logarithmic layer in the viscous boundary layer with the von Kármán constant $\kappa_u \approx 0.4$. For the thermal boundary layer in 2D, Zhu et al. (21) reported a log layer with $\kappa_T \approx 4.0$ in the plume-ejecting regions, but an absence of a log layer in the plume-impacting regions. These authors relate the observed logarithmic layers to an increase in the Nu scaling exponent from 0.30 to 0.38. In contrast, Iyer et al. (27) argued that "the boundary layers remain marginally stable and continue to act as the bottleneck for global heat transport," leading to classical 1/3 scaling.

We computed the boundary layer profiles for compressible convection, which are shown in Fig. 1. Here, we plot the normalized velocity (u^+) and normalized temperature (T^+) as a function of normalized vertical height (z^+) for the Bottom plate. Refer to *SI Appendix* and books (44, 46, 47) for the definitions of u^+, T^+, z^+. We observe logarithmic layers in u^+ and T^+ for 2D flows (Fig. 1 *A* and *C*), with the von Kármán constant κ_u ranging from 0.93 to 0.47 and κ_T ranging from 3.7 to 11 (Table 1). However, u^+ in 3D flows does not show a logarithmic layer, but T^+ does. Refer to *SI Appendix* for the parameters B_u and B_T and for the boundary layer properties of the top plate. The logarithmic layer observed in 2D convection may be caused by the horizontal sweeping flow, which is analogous to the behavior of flow past a flat plate. This sweeping flow is typically absent in 3D convection, which may explain the lack of a logarithmic layer in 3D (48). Most importantly, as we show in later discussion, $\mathrm{Nu} \sim \mathrm{Ra}^{0.30}$, regardless of whether a logarithmic layer is present.

Another interesting observation is that the free-slip RBC exhibits $\mathrm{Nu} \sim \mathrm{Ra}^{0.30}$ scaling despite the flow being turbulent everywhere and lacking a viscous boundary layer (29). Note that for large Ra, the bulk flow in RBC and compressible convection are turbulent irrespective of the nature of the boundary layers. These observations appear to weaken the connection between the logarithmic layer and the ultimate regime. This led us to explore heat fluxes in turbulent convection, which is the topic of the next subsections.

Anisotropic Heat Flux and Nusselt Number Scaling. In this subsection, we discuss the temperature and velocity fields and their correlations for the PC, RBC, and CC. We take a snapshot of PC at Ra of 10^7, a snapshot of RBC at Ra of 10^9, and a snapshot of CC at Ra of 10^9 under steady state, and display their central vertical cross-sections in Fig. 2 *A*–*C*. This figure contains the vector plots of the velocity field [$\mathbf{u}(\mathbf{r})$] and the density plots of the temperature field [$T(\mathbf{r})$, $T_{\mathrm{sa}}(\mathbf{r})$]. See Eq. **23** for the definition of superadiabatic temperature, $T_{\mathrm{sa}}(\mathbf{r})$. Note that $T_{\mathrm{sa}}(\mathbf{r}) < 0$ for CC (32). We compute the vertical heat flux $F_z(\mathbf{r})$ for the three vertical cross-sections and exhibit them in Fig. 2 *D*–*F*. Note that $F_z(\mathbf{r}) = u_z(\mathbf{r})T(\mathbf{r})$ for PC and RBC, whereas $F_z(\mathbf{r}) = \rho(\mathbf{r})u_z(\mathbf{r})T_{\mathrm{sa}}(\mathbf{r})$ for CC.

Before plunging into the heat flux of turbulent convection, we discuss the flux $\mathbf{F}(\mathbf{r}) = \mathbf{u}(\mathbf{r})\phi(\mathbf{r})$ for an isotropic scalar turbulence. Here, the isotropic velocity field $\mathbf{u}(\mathbf{r})$ advects the isotropic scalar field $\phi(\mathbf{r})$. For an isotropic turbulence, the ensemble-averaged flux $\langle \mathbf{F}(\mathbf{r}) \rangle = \langle \mathbf{u}(\mathbf{r})\phi(\mathbf{r}) \rangle = 0$ because $\mathbf{u}(\mathbf{r}) = \mathbf{a}$ and $-\mathbf{a}$ occur with equal probability for a given $\phi(\mathbf{r})$ (49, 50). Fig. 3*A* shows that in an isotropic passive turbulence, the average vertical flux, $\langle F_z \rangle = \langle u_z T \rangle$, is zero because positive and negative u_z values occur with equal probability for a given T.

In turbulent convection, buoyancy acts along the vertical direction, which breaks the isotropy. In PC, a hot thermal plume ($T > 0$) has $u_z > 0$, whereas a cold plume ($T < 0$) has $u_z < 0$, leading to predominantly positive F_z (Figs. 2 *A* and *D* and 3*B*). Note that the horizontal heat flux in convection vanishes due to the symmetry along the horizontal. RBC and CC have very different behaviors from PC. As shown in Fig. 2 *B*, *C*, *E*, and *F*, in RBC and CC, a hot packet has both positive and negative u_z, leading to positive and negative heat fluxes (F_{z+}, F_{z-}). However, F_{z+} wins over F_{z-} that yields a net positive heat flux. We illustrate these features in Fig. 3 *C* and *D*. Two-dimensional PC, RBC, and CC have very similar behavior, except that 2D flow structures are larger in size than the 3D counterparts, which is attributed to the inverse energy cascade in 2D convection (36) (*SI Appendix*). We remark that the above features are generic and are observed all the time.

We relate the average vertical heat flux ($\langle F_z \rangle$) to the Nusselt number (Nu). The total Nu gets contributions from the positive

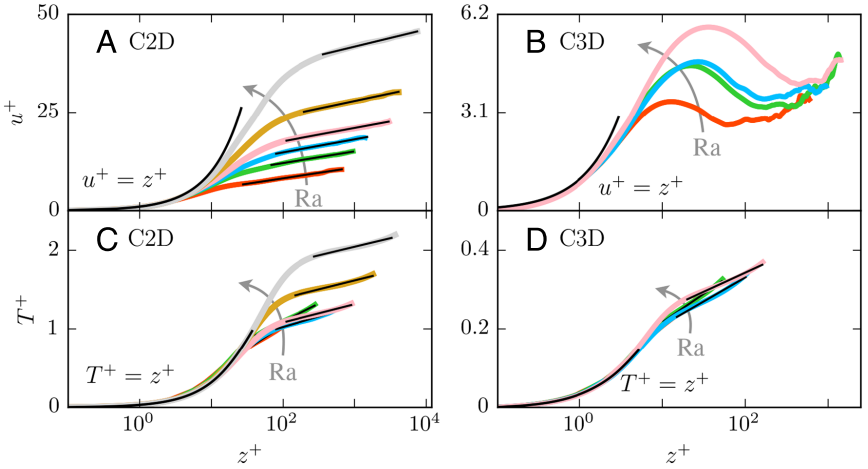

Fig. 1. For compressible convection near the *Bottom plate*, plots of u^+ vs. z^+ (*Top* row: *A* and *B*) and T^+ vs. z^+ (*Bottom* row: *C* and *D*). The *Left* column is for 2D with Ra = 10^{11} (red), 10^{12} (green), 10^{13} (blue), 10^{14} (pink), 10^{15} (golden), and 10^{16} (gray). With increasing Ra, the von Kármán constant κ_U varies from 0.83 to 0.47, whereas κ_T varies from 4 to 11. The *Right* column is for 3D convection with Ra = 10^{10} (red), 10^{11} (green), 10^{12} (blue), and 10^{13} (pink). Figure (*B*) does not exhibit a clear signature of a logarithmic layer. (*D*) For the thermal boundary layer in 3D, κ_T varies from 13 to 24.

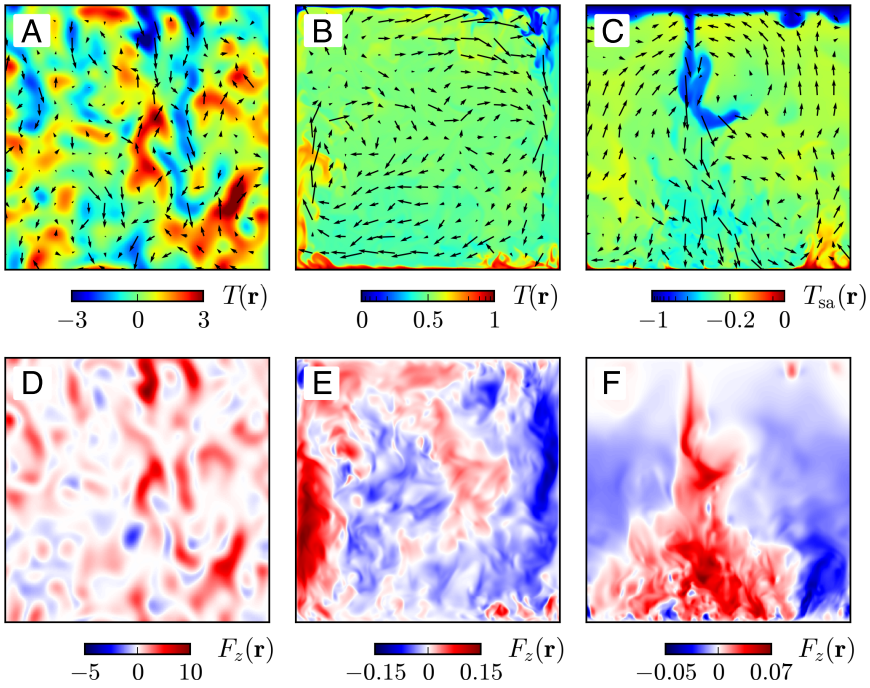

Fig. 2. Plots of the velocity and temperature fields (*A*–*C*), and vertical heat flux $F_Z(\mathbf{r})$ (*D*–*F*) in the mid vertical cross-section for (*A* and *D*) 3D periodic convection (PC) with Ra = 10^7; (*B* and *E*) 3D RBC with Ra = 10^9; (*C* and *F*) 3D compressible convection (CC) with Ra = 10^9. PC exhibits predominantly positive F_z, whereas RBC and CC exhibit both positive and negative F_z.

and negative heat fluxes, $\langle F_{z\pm}\rangle$. In terms of nondimensional u_z and T (or T_{sa} for CC) (31, 32),

$$\begin{aligned}\mathrm{Nu} &= 1+\sqrt{\mathrm{RaPr}}[\langle F_{z+}\rangle+\langle F_{z-}\rangle]\\ &= 1+\sqrt{\mathrm{RaPr}}[\langle (u_zT)_+\rangle+\langle (u_zT)_-\rangle] \text{ in RBC \& PC,}\end{aligned} \quad [1]$$

$$\begin{aligned}\mathrm{Nu} &= 1+\sqrt{\mathrm{RaPr}}[\langle F_{z+}\rangle+\langle F_{z-}\rangle]\\ &= 1+\sqrt{\mathrm{RaPr}}[\langle (\rho u_zT_{sa})_+\rangle+\langle (\rho u_zT_{sa})_-\rangle] \text{ in CC.}\end{aligned} \quad [2]$$

In Eq. **2**, we ignore the contributions from the kinetic energy flux, which is negligible (32). Eq. **1** yields satisfactory Nu for PC, but Eqs. **1** and **2** exhibit significant fluctuations for RBC and CC, for which we compute Nu using the temperature gradient in the boundary layer as follows (5, 21, 32):

$$\mathrm{Nu} = -\frac{1}{2}\left[\left.\frac{d\langle T\rangle_{A,t}}{dz}\right|_{z=0}+\left.\frac{d\langle T\rangle_{A,t}}{dz}\right|_{z=1}\right] \text{ in RBC,} \quad [3]$$

$$\mathrm{Nu} = -\frac{1}{2}\left[\left.\frac{d\langle T_{sa}\rangle_{A,t}}{dz}\right|_{z=0}+\left.\frac{d\langle T_{sa}\rangle_{A,t}}{dz}\right|_{z=1}\right] \text{ in CC.} \quad [4]$$

Note that Nu computed at the boundaries using Eqs. **3** and **4** matches with those computed using Eqs. **1** and **2**, provided significant averaging is performed for the latter.

We compute Nu for PC, RBC, and CC using Eqs. **1**, **3**, and **4**, respectively. We average over 700 to 10,000 dataframes for these computations. To test Nu scaling, we fit the data with $\mathrm{Nu} = a\mathrm{Ra}^b$ using Python's polyfit function. The prefactor a and the exponent b for all the runs are listed in Table 2. Fig. 4*A* exhibits the normalized Nu, NuRa^{-b}, for periodic convection (P2D and P3D: thin and thick red lines), RBC (R2D and R3D: thin and thick green lines), and compressible convection (C2D

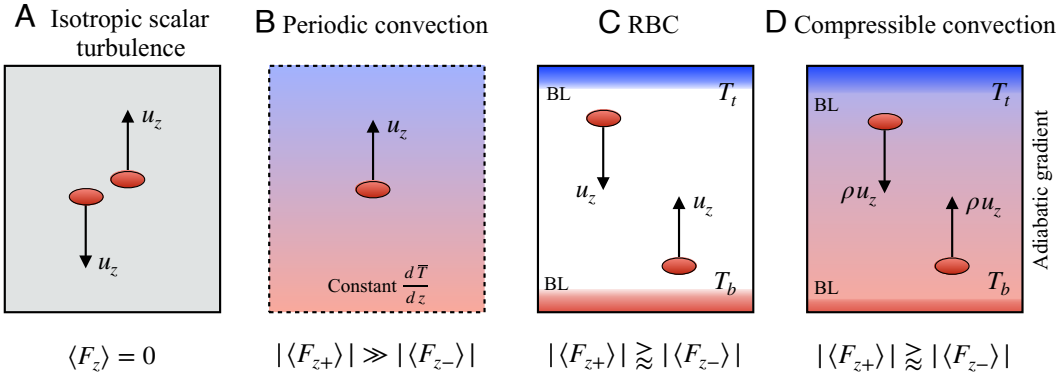

Fig. 3. Schematic diagrams illustrating heat fluxes: (*A*) In isotropic scalar turbulence, a thermal packet is equally likely to move up and down, which leads to $\langle F_z\rangle = 0$; (*B*) In periodic convection, a hot plume predominantly rises, which leads to $|\langle F_{z+}\rangle| \gg |\langle F_{z-}\rangle|$; (*C* and *D*) In RBC and compressible convection, some hot fluids have positive u_z, while others have negative u_z. This leads to $|\langle F_{z+}\rangle| \gtrapprox |\langle F_{z-}\rangle|$.

Table 2. Scaling of the Nusselt number, Nu, and absolute values of the averaged and normalized positive and negative heat fluxes ($|\langle F_{z+}\rangle|$, $|\langle F_{z-}\rangle|$) for periodic convection (P2D, P3D), RBC (R2D, R3D), and compressible convection (C2D, C3D)

System	Nu	$\lvert\langle F_{z+}\rangle\rvert$	$\lvert\langle F_{z-}\rangle\rvert$
P2D	$(0.87 \pm 0.30)\mathrm{Ra}^{(0.50 \pm 0.025)}$	$(1.79 \pm 0.35)\mathrm{Ra}^{(0.022 \pm 0.014)}$	$(0.43 \pm 0.10)\mathrm{Ra}^{(0.044 \pm 0.017)}$
P3D	$(1.23 \pm 0.32)\mathrm{Ra}^{(0.47 \pm 0.02)}$	$(2.42 \pm 0.25)\mathrm{Ra}^{(-0.030 \pm 0.008)}$	$(0.28 \pm 0.023)\mathrm{Ra}^{(0.003 \pm 0.006)}$
R2D	$(0.11 \pm 0.011)\mathrm{Ra}^{(0.29 \pm 0.003)}$	$(0.18 \pm 0.046)\mathrm{Ra}^{(-0.025 \pm 0.009)}$	$(0.16 \pm 0.043)\mathrm{Ra}^{(-0.021 \pm 0.009)}$
R3D	$(0.16 \pm 0.063)\mathrm{Ra}^{(0.28 \pm 0.022)}$	$(0.092 \pm 0.014)\mathrm{Ra}^{(-0.038 \pm 0.009)}$	$(0.045 \pm 0.007)\mathrm{Ra}^{(-0.009 \pm 0.009)}$
C2D	$(0.028 \pm 0.004)\mathrm{Ra}^{(0.32 \pm 0.005)}$	$(0.019 \pm 0.005)\mathrm{Ra}^{(0.018 \pm 0.009)}$	$(0.011 \pm 0.004)\mathrm{Ra}^{(0.033 \pm 0.011)}$
C3D	$(0.047 \pm 0.009)\mathrm{Ra}^{(0.31 \pm 0.008)}$	$(0.079 \pm 0.007)\mathrm{Ra}^{(-0.10 \pm 0.004)}$	$(0.027 \pm 0.005)\mathrm{Ra}^{(-0.070 \pm 0.008)}$

See Eqs. **1** and **2**.

and C3D: thin and thick blue lines). Clearly, $\mathrm{Nu} \sim \mathrm{Ra}^{1/2}$ for the PC, but $\mathrm{Nu} \sim \mathrm{Ra}^{0.3}$ for RBC and CC. The figure also illustrates that for a given Ra, Nu(PC) > Nu(RBC) > Nu(CC). In addition, for most cases, Nu for 3D is larger than that for 2D, possibly because of two pathways (*xz* and *yz*) for 3D flows compared to a single pathway (*xz*) for 2D flows. Also, Nu in 2D convection shows stronger fluctuations (or error bars) than in 3D convection, which is due to the inverse energy cascade in 2D (36). An important observation, Eqs. **1** and **2** and the Nu scaling reveal that $\langle F_z\rangle \sim \mathrm{NuRa}^{-1/2} \sim \mathrm{Ra}^{b-1/2}$. Hence, the normalized flux decreases as $\langle F_z\rangle \sim \mathrm{Ra}^{-0.2}$ for RBC and CC, but it remains constant for PC. The *Insets* of Fig. 4*B* illustrate $\langle F_z\rangle$ for P2D, P3D, R3D, and C3D; we exclude R2D and C2D because they exhibit strong fluctuations. We will explore the reasons for such behavioral differences in PC, RBC, and CC by examining the heat fluxes $\langle F_{z\pm}\rangle$.

We compute $\langle F_{z\pm}\rangle$ using the numerical data and observe that $\langle F_{z\pm}\rangle \approx a_{\pm}\mathrm{Ra}^{b_{\pm}}$. In Fig. 4*B*, the red, green, and blue squares and circles represent positive heat fluxes in 2D and 3D, respectively, whereas pentagons and triangles represent the respective negative heat fluxes. Regarding the best-fit curves, the thin and thick solid lines represent positive fluxes for 2D and 3D, respectively. The dashed lines represent the respective negative fluxes. The plots in the figure reveal the following insights:

1. For PC, $\langle F_{z+}\rangle$ is several times larger than $\langle F_{z-}\rangle$, consistent with Figs. 2*D* and 3*B*. In addition, $\langle F_{z+}\rangle$ for 2D increases marginally with Ra, but $\langle F_{z+}\rangle$ for 3D decreases marginally with Ra.
2. In 3D RBC and CC, both $\langle F_{z+}\rangle$ and $\langle F_{z-}\rangle$ decrease with Ra, but the former decreases more rapidly than the latter. This feature leads to $\langle F_z\rangle \sim \langle F_{z+}\rangle + \langle F_{z-}\rangle \sim \mathrm{Ra}^{-0.20}$ or $\mathrm{Nu} \sim \mathrm{Ra}^{1/2-0.20} \sim \mathrm{Ra}^{0.30}$, consistent with experimental and numerical observations.
3. In 2D RBC, both $\langle F_{z+}\rangle$ and $\langle F_{z-}\rangle$ decrease marginally with Ra, with $\langle F_{z+}\rangle$ decreasing slightly faster than $\langle F_{z-}\rangle$. In CC, both $\langle F_{z+}\rangle$ and $\langle F_{z-}\rangle$ increase marginally with Ra, but $\langle F_{z-}\rangle$ increases slightly faster than $\langle F_{z+}\rangle$. However, the difference $\langle F_{z+}\rangle + \langle F_{z-}\rangle \sim \mathrm{Ra}^{-0.20}$ or $\mathrm{Nu} \sim \mathrm{Ra}^{1/2-0.20} \sim \mathrm{Ra}^{0.30}$.

Thus, a complex interplay of $\langle F_{z+}\rangle$ and $\langle F_{z-}\rangle$ yields $\mathrm{Nu} \sim \mathrm{Ra}^{0.3}$ scaling. This result is independent of the presence or absence of a logarithmic layer in the boundaries. We will continue this discussion in the next subsection.

PDF of Turbulent Convection. Further, we compute the probability distribution function (PDF) of the heat flux, $P(F_z)$, by averaging over 8 to 20 datasets. In Fig. 5, we plot $P(F_z)$ for selected Ra's among PC, CC, and RBC. Note that Fig. 5 *A*, *B*, *D*, and *F* are plotted on a semilogy scale, whereas Fig. 5 *C* and *E* are plotted on log–log scale. We chose the latter scale because $P(F_z)$ for 2D RBC and CC drops sharply with F_z. As we describe below, the $P(F_z)$ plots reveal interesting patterns and bolster the arguments for classical Nu scaling.

Periodic convection. For PC, $P(F_z)$, primarily dominated by positive F_z, is nearly Gaussian near the peak of the PDF, but it exhibits significant rightward skewness, particularly in 3D. As Ra increases, the tails of $P(F_z)$ become more extended for

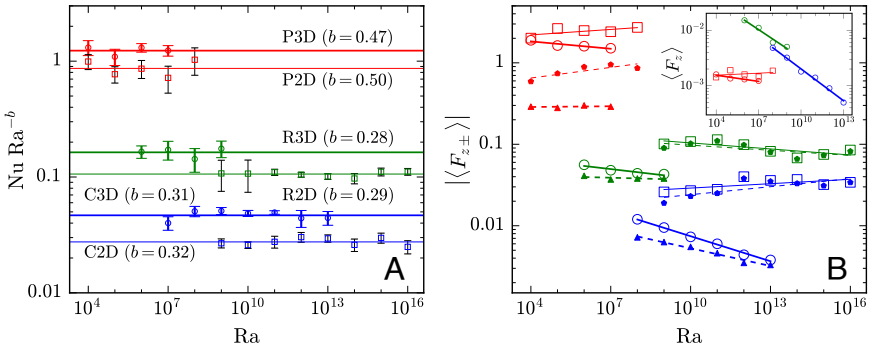

Fig. 4. (*A*) Plots of normalized Nusselt number NuRa^{-b} vs. Ra for 2D (squares, thin lines) and 3D (circles, thick lines) simulations. Red for periodic convection (P2D, P3D), green for RBC (R2D, R3D), and blue for compressible convection (C2D, C3D). Here, the symbols squares and circles represent the numerical data, while the straight lines represent the best-fit curves. (*B*) Plots of convective heat fluxes $|\langle F_{z\pm}\rangle|$ vs. Ra with the same color convention as (*A*). In (*B*), the squares and circles denote positive fluxes in 2D and 3D, respectively; the pentagons and triangles represent the respective negative fluxes; solid and dashed lines represent best-fit curves for F_{z+} and F_{z-}, respectively. The thin and thick lines distinguish between 2D and 3D curves, respectively. The *Inset* in (*B*) illustrates $\langle F_z\rangle$ scaling for P2D, P3D, R3D, and C3D; we skip R2D and C2D data because they exhibit strong fluctuations.

2D, but less extended for 3D. These observations are consistent with $|\langle F_z \rangle|$ increasing marginally with Ra in 2D, but decreasing marginally with Ra in 3D.

RBC and compressible convection. The PDFs for 3D RBC and CC, shown in Fig. 5 *D* and *F*, exhibit longer tails for F_{z+} than for F_{z-}, which leads to $\langle F_{z+} \rangle > \langle F_{z-} \rangle$ or positive Nu. As Ra increases, the tails of the PDFs shrink and the difference $\Delta P = P(F_z) - P(-F_z)$ decreases. These features lead to the decrease of $\langle F_z \rangle$ as $\mathrm{Ra}^{-0.20}$, as shown in Fig. 4*B*.

As shown in Fig. 5, the PDFs of 2D RBC and CC are more symmetric than their 3D counterparts, leading to $\Delta P = P(F_z) - P(-F_z)$ either being small or fluctuating around zero in 2D convection (see *Insets* of Fig. 5 *C* and *E*). In addition, the 2D PDFs exhibit stronger fluctuations and longer tails than 3D PDFs, primarily due to the inverse energy cascade in 2D flows (36) and due to differences in vortex dynamics in 2D and 3D (41). Consequently, $\langle F_z \rangle$ and the bulk-averaged Nu ($\mathrm{Ra}^{1/2}\langle F_z \rangle$) exhibit strong fluctuations, consistent with earlier observations by Samuel and Verma (36), Pandey and Sreenivasan (51), and Lindborg (52). Note, however, that the Nu scaling for 2D and 3D RBC and CC are very similar, even though 2D and 3D convection have different properties.

Thus, the asymmetric heat fluxes, their PDFs, and Nusselt number scaling provide a consistent picture leading to the classical Nu scaling.

Discussions

In thermal convection, we expect a hot plume to ascend and a cold plume to descend, which would yield a positive heat flux. However, our study reveals that the above dynamics occur only in PC (Fig. 3*B*). With $F_{z+} \gg F_{z-}$, Eq. **1** yields

$$\begin{aligned} \mathrm{Nu} &\approx \sqrt{\mathrm{RaPr}}\langle F_{z+} \rangle \approx \sqrt{\mathrm{RaPr}}\langle (u_z T)_+ \rangle \\ &\approx \sqrt{\mathrm{RaPr}} u_{z,\mathrm{rms}} T_{\mathrm{rms}} \sim \sqrt{\mathrm{RaPr}}. \end{aligned} \quad [5]$$

PC exhibits the above Nu scaling because u_z and T are strongly correlated in such flows, with the nondimensional $u_{z,\mathrm{rms}} \approx 1$ and $T_{\mathrm{rms}} \approx 1$.

In contrast, RBC and CC exhibit both positive and negative heat fluxes. The negative flux arises due to the thermal plates, e.g., the top plate deflects the hot plumes downward, leading to negative flux (Fig. 3 *C* and *D*). We find that $P(F_z)$ is symmetrical around $F_z = 0$ for small $|F_z|$, but positive F_z has a longer tail than negative F_z. Hence, $|\langle F_{z+} \rangle| \gtrapprox |\langle F_{z-} \rangle|$. As shown in Fig. 4, the net $\langle F_z \rangle \sim \mathrm{Ra}^{-0.20}$, which leads to (for $\mathrm{Pr} \approx 1$)

$$\mathrm{Nu} \approx \sqrt{\mathrm{RaPr}}[\langle F_{z+} \rangle + \langle F_{z-} \rangle] \sim \sqrt{\mathrm{RaPr}}\mathrm{Ra}^{-0.20} \sim \mathrm{Ra}^{0.30}. \quad [6]$$

The above scaling for the flux correlation has been reported earlier (6, 28), and they are independent of the nature of boundary

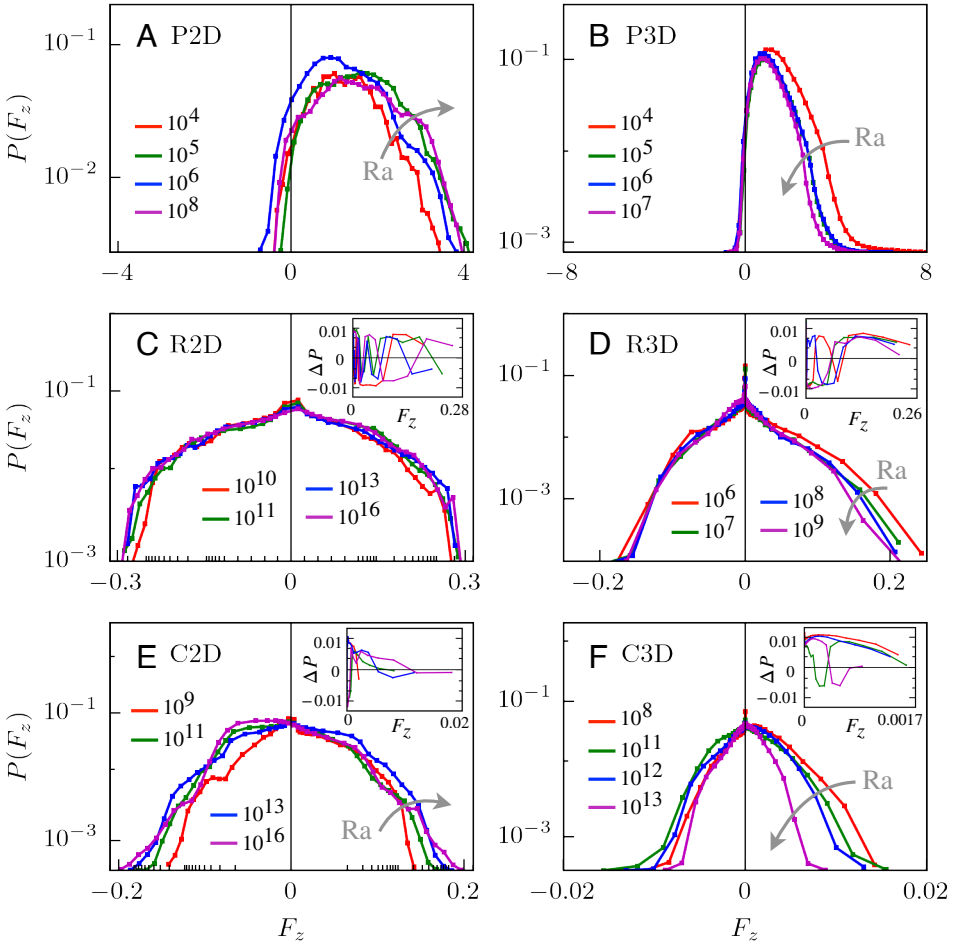

Fig. 5. Probability distribution function ($P(F_z)$) of the normalized heat flux F_z: (*A* and *B*) 2D and 3D periodic convection (P2D, P3D); (*C* and *D*) 2D and 3D RBC (R2D, R3D); and (*E* and *F*) 2D and 3D compressible convection (C2D, C3D). Subplots (*C* and *E*) are in log–log scale, while others are in semilogy scale. The *Insets* show the $\Delta P = P(F_z) - P(-F_z)$ vs. F_z plots in semilogy scale.

layers. Thus, in turbulent convection with thermal plates, $\langle u_z T\rangle$ is neither zero (as in isotropic scalar turbulence) nor $(u_z)_{\rm rms} T_{\rm rms}$ (as in periodic convection), which is a result of coexistence of F_{z+} and F_{z-}.

Many researchers (17, 20, 45) attempted to relate the possible ultimate-regime scaling in turbulent RBC to the flow past a flat plate, where the boundary layer turns turbulent near Reynolds number $\mathrm{Re}_c = 5\times10^5$. Using $\mathrm{Re}\approx 0.1\sqrt{\mathrm{Ra}}$ (27), the transition to turbulence in RBC is estimated to occur near $\mathrm{Ra}\approx 10^{14}$. Beyond this Ra, the boundary layers and the bulk fluid are expected to exhibit turbulent behavior. However, there are critical differences between RBC and flow past a flat plate. The boundary layer of a flat plate undergoes a transition from laminar to turbulent flow as one progresses downstream; however, such a distinct evolution is not evident in thermal convection. Also, for a flat plate, the bulk flow above the turbulent boundary layer is typically streamlined. In contrast, for $\mathrm{Ra}\gtrapprox 10^7$, the bulk flow in convection is turbulent regardless of the boundary layer's nature. Given this, the analogy between flow past a flat plate and turbulent convection is tenuous. Interestingly, the classical 1/3 scaling appears for a range of Ra (from 10^7 to 10^{16}) in RBC with no-slip and free-slip boundary conditions, with the latter flow being turbulent everywhere without any viscous boundary layer. Thus, the Nu scaling is marginally connected with the nature of the velocity boundary layer. Instead, the wall-induced $u_z T$ correlation, along with the positive and negative heat fluxes, appear to play a critical role in classical 1/3 scaling for turbulent convection.

There are several examples that need attention in view of heat flux asymmetry. Bouillaut et al. (53) and Lepot et al. (54) observed ultimate-regime scaling for convection driven by internal heat sources, internal heat sinks, and radiative heating. Turbulent convection with rough walls too exhibits ultimate-regime scaling (55). Additionally, convection driven by a horizontal pressure gradient exhibits an enhanced Nu exponent (up to 0.45) for large horizontal shear (56, 57). We conjecture that, in the above examples, the internal heat sources and sinks, horizontal shear, and rough walls increase the positive heat fluxes over the negative ones, leading to an enhancement of the Nu scaling exponent. We plan to test the above conjecture.

Conclusions

Despite extensive research, modeling heat transport in turbulent convection continues to be a significant hurdle. The two competing theories are classical Nu scaling (1/3) and ultimate-regime scaling (1/2). Some researchers argue that the Nu scaling exponent grows from 1/3 to higher values near $\mathrm{Ra}\approx 10^{14}$, where the boundary layer becomes turbulent and a logarithmic layer emerges. However, other researchers dispute these claims. As discussed in the previous section, the relation between the turbulent boundary layer and the emergence of the ultimate regime appears to be weak. In this paper, we take a different path and address this issue using turbulent heat flux (F_z).

We analyzed the positive and negative heat fluxes in 28 numerical datasets of RBC and CC whose Rayleigh numbers range from 10^6 to 10^{16}. Our analysis shows that RBC and CC exhibit both positive and negative heat fluxes, with a nearly symmetric PDF of heat flux, $P(F_z)$. A small asymmetry in $P(F_z)$ results in a net heat flux scaling of $\langle F_z\rangle \sim \mathrm{Ra}^{-0.20}$, which leads to $\mathrm{Nu}\sim \mathrm{Ra}^{1/2-0.20}\sim \mathrm{Ra}^{0.30}$. This phenomenon is quite robust, especially considering that the boundary layer in compressible convection simulations exhibits a logarithmic layer, while those in RBC simulations are uncertain. This robust classical scaling aligns with the models presented by Malkus (8) and Priestley (7). We expect the above heat flux behavior to persist for extreme Ra's (e.g., 10^{20} and beyond), but testing this conjecture will require enormous computing resources.

In contrast, periodic convection has an asymmetric heat flux with a dominant positive component. Periodic convection exhibits $\mathrm{Nu}\sim \mathrm{Ra}^{1/2}$, similar to that in the ultimate regime. We associate the difference between the 1/2 and 1/3 Nu scaling to the thermal plates. For example, the upper plate deflects the hot plumes downward, which yields negative heat flux. Absence of such wall effects in periodic convection yields dominantly positive heat flux. Thus, our paper clearly contrasts isotropic scalar turbulence, periodic convection, RBC, and compressible convection (Fig. 3).

In summary, this paper offers important insights into a long-standing problem of turbulent convection, indicating a likely absence of the ultimate regime. We demonstrate that the classical Nu scaling possibly occurs due to the positive and negative heat fluxes induced by thermal plates. Note, however, that convection with rough walls or internal heat sources and sinks yields ultimate-regime scaling. It would be interesting to explore how these factors affect heat fluxes. In addition, analyzing asymmetric momentum fluxes around airplane wings, in pipes, and in nozzles may provide valuable insights into the drag reduction and relaminarization observed in such systems (44, 58).

Materials and Methods

In this section, we briefly describe the numerical methods used to simulate periodic convection, RBC, and compressible convection.

Periodic Convection. We simulate 2D periodic convection in a $(2\pi)^2$ periodic box and 3D convection in a $(2\pi)^3$ periodic box for the parameters listed in Table 1. We solve the following nondimensionalized equations numerically (28, 33):

$$\frac{\partial \mathbf{u}}{\partial t} + \mathbf{u}\cdot\nabla\mathbf{u} = -\nabla p + T'\hat{z} + \sqrt{\frac{\mathrm{Pr}}{\mathrm{Ra}}}\nabla^2\mathbf{u}, \quad [7]$$

$$\frac{\partial T'}{\partial t} + \mathbf{u}\cdot\nabla T' = u_z + \frac{1}{\sqrt{\mathrm{Ra}\,\mathrm{Pr}}}\nabla^2 T', \quad [8]$$

$$\nabla\cdot\mathbf{u} = 0, \quad [9]$$

where temperature $T = \bar{T} + T'$ with $\bar{T} = 1 - z/(2\pi)$ as the linear background profile and T' as perturbation. The Rayleigh number and Prandtl number are defined as

$$\mathrm{Ra} = \frac{d\bar{T}}{dz}\frac{\alpha g d^4}{\nu\kappa}, \quad \mathrm{Pr} = \frac{\nu}{\kappa}, \quad [10]$$

where α is the thermal expansion coefficient, ν is the kinematic viscosity, κ is the thermal diffusivity, g is the gravitational acceleration, d is the height of the box, and $d\bar{T}/dz$ is the mean temperature gradient. The velocity field $\mathbf{u}$ and the temperature fluctuations T' satisfy periodic boundary conditions.

The above equations are solved numerically using the pseudospectral GPU-enabled code Tarang-py (40). We employ the fourth-order Runge–Kutta (RK4) time-stepping scheme, as well as hypodiffusive term $10^{-2}\nabla^{-1}$ and hyperdiffusive term $10^{-8}\nabla^8$ to both $\mathbf{u}$ and T' in order to stabilize the elevator modes (34, 59). All our simulations are well resolved, with $\mathcal{R}_\eta > 1$ in each case. Refer to Table 1 for the simulation parameters, Re, Pr, Nu, $\mathcal{R}_\eta$, etc.

Rayleigh-Bénard Convection. The 2D RBC datasets have been taken from Samuel and Verma (36) and Samuel (37), whereas the 3D datasets have been taken from Bhattacharya et al. (35). The above authors solved the following nondimensionalized equations:

$$\frac{\partial \mathbf{u}}{\partial t} + \mathbf{u}\cdot\nabla\mathbf{u} = -\nabla p + T\hat{z} + \sqrt{\frac{\mathrm{Pr}}{\mathrm{Ra}}}\nabla^2\mathbf{u}, \quad [11]$$

$$\frac{\partial T}{\partial t} + \mathbf{u}\cdot\nabla T = \frac{1}{\sqrt{\mathrm{Ra}\,\mathrm{Pr}}}\nabla^2 T, \quad [12]$$

$$\nabla\cdot\mathbf{u} = 0, \quad [13]$$

where $\mathbf{u}$, p, and T are the velocity, pressure, and temperature fields, respectively. Here, a fluid is confined between two horizontal plates separated by a unit distance. The horizontal extent of the fluid is Γ, the aspect ratio. The bottom and top plates are maintained at temperatures 1 and 0, respectively. The Rayleigh number and Prandtl number for RBC are defined as

$$\mathrm{Ra} = \frac{\alpha(\Delta T)gd^3}{\nu\kappa}, \quad \mathrm{Pr} = \frac{\nu}{\kappa}, \quad [14]$$

where ΔT is the imposed temperature difference across the plates. Ra, Pr, Γ, Re, Nu, $\mathcal{R}_\eta$, etc. are listed in Table 1.

Samuel and Verma (36), Samuel (37), and Bhattacharya et al. (35) employed the finite-difference code SARAS (43). The solver uses a multigrid method for the pressure-Poisson equation and a second-order Crank-Nicolson scheme for time stepping. For the top and bottom boundaries, both 2D and 3D runs employ no-slip boundary conditions for the velocity field and conducting boundary conditions for the temperature field. However, for the side walls, the 2D simulations employ periodic boundaries, while the 3D simulations employ no-slip and adiabatic boundary conditions. For all the runs, the grid spacing is smaller than the Kolmogorov length scale $\eta = \langle \nu^3/\epsilon_u\rangle^{1/4}$, where $\epsilon_u = (\nu/2)\langle(\partial_i u_j + \partial_j u_i)^2\rangle$ is the kinetic energy dissipation rate. This condition ensures that the resolution parameter $\mathcal{R}_\eta > 1$, as listed in Table 1. The boundary layers are well resolved with at least 5 grid points, satisfying the Grötzbach criterion (60).

Compressible Convection. We simulate compressible convection in a box of dimension $\Gamma \times 1$ in 2D and $\Gamma \times \Gamma \times 1$ in 3D. The bottom plate is maintained at unit temperature, whereas the top plate at $1 - D - \epsilon$, where ϵ and D are the superadiabaticity and the dissipation number, defined below

$$\epsilon = \frac{d}{T_b}\left(\frac{\Delta T}{d} - \frac{g}{C_p}\right), \quad D = \frac{gd}{T_b C_p}. \quad [15]$$

The Rayleigh number and Prandtl number are defined as (38, 39)

$$\mathrm{Ra} = \frac{\epsilon g d^3}{\nu\kappa}, \quad \mathrm{Pr} = \frac{\nu}{\kappa}. \quad [16]$$

The horizontal plates are maintained at a constant temperature (conducting boundary condition). In addition, we set $\mathbf{u} = 0$ on the horizontal plates. Periodic boundary condition is applied for the vertical walls. We solve the following nondimensional equations in conservative form (38, 39):

$$\frac{\partial \rho}{\partial t} + \frac{\partial}{\partial x_i}(\rho u_i) = 0, \quad [17]$$

$$\frac{\partial}{\partial t}(\rho u_i) + \frac{\partial}{\partial x_j}(\rho u_i u_j + \delta_{ij} p - \tau_{ij}) = -\frac{1}{\epsilon}\rho\delta_{iz}, \quad [18]$$

$$\frac{\partial E}{\partial t} + \frac{\partial}{\partial x_i}\left(u_i(E+p) - \frac{1}{\epsilon D\sqrt{\mathrm{Ra}\,\mathrm{Pr}}}\frac{\partial T}{\partial x_i} - u_j\tau_{ij}\right) = 0, \quad [19]$$

where $\mathbf{u}$ and T are the nondimensional velocity and temperature fields, respectively; and ρ is the nondimensional density field. The nondimensional pressure for an ideal gas is

$$p = (\gamma - 1)\frac{\rho T}{\gamma\epsilon D}, \quad [20]$$

where $\gamma = C_p/C_v$ is the ratio of specific heat capacities. The viscous stress tensor is given by

$$\tau_{ij} = \sqrt{\frac{\mathrm{Pr}}{\mathrm{Ra}}}\left(\partial_j u_i + \partial_i u_j - \frac{2}{3}\partial_m u_m \delta_{ij}\right), \quad [21]$$

and the total energy density is

$$E = \rho\left(\frac{u^2}{2} + \frac{T}{\gamma\epsilon D} + \frac{z}{\epsilon}\right). \quad [22]$$

Note that the background adiabatic profile is $T_A(z) = 1 - Dz$, and the superadiabatic temperature is defined as

$$T_{\mathrm{sa}}(\mathbf{r}) = \frac{T(\mathbf{r}) - T_A(z)}{\epsilon}, \quad [23]$$

which measures the deviation of temperature from the adiabatic state, normalized by the superadiabaticity. Refer to Spiegel (38) and Graham (39) for details on compressible equations.

We solve Eqs. **17**–**19** using the finite-difference solver Dhara (32), which employs the MacCormack-TVD (Total Variation Diminishing) scheme on a collocated grid (61, 62). The MacCormack scheme is second-order accurate in both space and time (61). A nonuniform tangent-hyperbolic grid is employed in the z-direction to enhance resolution near the boundaries, while uniform grids are used in the x and y directions. At the top and bottom plates, second-order forward and backward finite differences are used to evaluate boundary values, respectively. The general conservative form of the governing equations is written as

$$\frac{\partial Q}{\partial t} + \frac{\partial F_i}{\partial x_i} = S_i, \quad [24]$$

where Q is a generic conserved variable; F_i is the flux; and S_i is the source term in the i-direction. Using operator splitting, Eq. **24** is decomposed into three one-dimensional subproblems, each solved using the MacCormack predictor–corrector approach. The TVD correction is added to suppress spurious oscillations and preserve monotonicity in steep-gradient regions (62). For further details, see ref. 32.

All our simulations are well resolved, with the resolution parameter $\mathcal{R}_\eta = \min_i(\eta(z)/\Delta x_i) > 0.5$ (30, 63) (Table 1). The Kolmogorov length scale is given by $\eta(z) = (\nu^3\langle\rho\rangle/\langle S_{ij}\tau_{ij}\rangle)^{1/4}$, where $S_{ij} = (\partial_i u_j + \partial_j u_i)/2$ is the strain-rate tensor. For all our runs, the boundary layers are resolved with at least 7 grid points, thus satisfying the Grötzbach criterion (60). For our numerical simulations, we fix $\gamma = 1.3, D = 0.5, \epsilon = 0.1$, Pr = 0.7, and vary Ra from 10^9 to 10^{16} for 2D, and from 10^7 to 10^{13} for 3D. See Table 1 for details. We perform our parallel runs on several GPUs that enable high-resolution simulations in a reasonable time. For instance, our largest 3D simulation on $501^2 \times 5{,}001$ grid ran for 10 d on the Kotak school's server (with 8 NVIDIA H100 GPUs), while the largest 2D run on $24{,}001^2$ grid ran for 20 d on two nodes of Sophia (with 8 NVIDIA A100 GPUs each) at Argonne National Laboratory.

Data, Materials, and Software Availability. Data and scripts are available at Zenodo (64).

ACKNOWLEDGMENTS. We thank K. R. Sreenivasan and Jörg Schumacher for valuable comments and suggestions and for careful reading of the manuscript. We thank Roshan Samuel and Shashwat Bhattacharya for providing the Rayleigh-Bénard convection datasets, and Rajesh Ranjan, Dhananjay Singh, and Sanjiva Lele for valuable discussions. Simulations were performed on the Argonne Leadership Computing Facility through the Director's Discretionary Program, and on the High-Performance Computing cluster of the Kotak School of Sustainability, Indian Institute of Technology Kanpur. L.S. thanks Indian Institute of Technology Kanpu for the Institute Postdoctoral Fellowship. Part of this work was done in the Center for Turbulence Research, Stanford University, where M.K.V. was a Visiting Senior Fellow. Part of this work was supported by Anusandhan National Research Foundation, India (Grant Nos. SERB/PHY/2021522 and SERB/PHY/2021473), and the J. C. Bose Fellowship (SERB /PHY/2023488).

1. E. D. Siggia, High Rayleigh number convection. *Annu. Rev. Fluid Mech.* **26**, 137–168 (1994).
2. G. Ahlers, S. Grossmann, D. Lohse, Heat transfer and large scale dynamics in turbulent Rayleigh-Bénard convection. *Rev. Mod. Phys.* **81**, 503–537 (2009).
3. D. Lohse, K. Q. Xia, Small-scale properties of turbulent Rayleigh-Bénard convection. *Annu. Rev. Fluid Mech.* **42**, 335–364 (2010).
4. J. Schumacher, K. R. Sreenivasan, Colloquium: Unusual dynamics of convection in the Sun. *Rev. Mod. Phys.* **92**, 041001 (2020).
5. F. Chillà, J. Schumacher, New perspectives in turbulent Rayleigh-Bénard convection. *Eur. Phys. J. E* **35**, 58 (2012).
6. M. K. Verma, *Physics of Buoyant Flows: From Instabilities to Turbulence* (World Scientific, Singapore, 2018).
7. C. Priestley, Convection from a large horizontal surface. *Aust. J. Phys.* **7**, 176–201 (1954).
8. W. V. R. Malkus, The heat transport and spectrum of thermal turbulence. *Proc. R. Soc. Lond. A* **225**, 196–212 (1954).
9. R. H. Kraichnan, Turbulent thermal convection at arbitrary Prandtl number. *Phys. Fluids* **5**, 1374–1389 (1962).
10. L. N. Howard, Heat transport by turbulent convection. *J. Fluid Mech.* **17**, 405–432 (1963).
11. E. A. Spiegel, A generalization of the mixing-length theory of turbulent convection. *Astrophys. J.* **138**, 216 (1963).
12. E. A. Spiegel, Convection in stars: I. Basic Boussinesq convection. *Annu. Rev. Astron. Astrophys.* **9**, 323–352 (1971).
13. L. N. Howard, "Convection at high Rayleigh number" in *Applied Mechanics: Proceedings of the Eleventh International Congress of Applied Mechanics Munich (Germany) 1964*, H. Görtler, Ed. (Springer, 1966), pp. 1109–1115.
14. P. P. Shevkar *et al*., Hierarchical network of thermal plumes and their dynamics in turbulent Rayleigh-Bénard convection. *Proc. Natl. Acad. Sci. U.S.A.* **122**, e2502972122 (2025).
15. C. R. Doering, F. Otto, M. G. Reznikoff, Bounds on vertical heat transport for infinite-Prandtl-number Rayleigh-Bénard convection. *J. Fluid Mech.* **560**, 229–241 (2006).
16. B. I. Shraiman, E. D. Siggia, Heat transport in high-Rayleigh-number convection. *Phys. Rev. A* **42**, 3650–3653 (1990).
17. S. Grossmann, D. Lohse, Scaling in thermal convection: A unifying theory. *J. Fluid Mech.* **407**, 27–56 (2000).
18. C. R. Doering, Turning up the heat in turbulent thermal convection. *Proc. Natl. Acad. Sci. U.S.A.* **117**, 9671–9673 (2020).
19. X. Chavanne, F. Chillà, B. Chabaud, B. Castaing, B. Hebral, Turbulent Rayleigh-Bénard convection in gaseous and liquid He. *Phys. Fluids* **13**, 1300–1320 (2001).
20. X. He, D. Funfschilling, H. Nobach, E. Bodenschatz, G. Ahlers, Transition to the ultimate state of turbulent Rayleigh-Bénard convection. *Phys. Rev. Lett.* **108**, 024502 (2012).
21. X. Zhu, V. Mathai, R. J. A. M. Stevens, R. Verzicco, D. Lohse, Transition to the ultimate regime in two-dimensional Rayleigh-Bénard convection. *Phys. Rev. Lett.* **120**, 144502 (2018).
22. D. Lohse, O. Shishkina, Ultimate Rayleigh-Bénard turbulence. *Rev. Mod. Phys.* **96**, 035001 (2024).
23. O. Shishkina, D. Lohse, Ultimate regime of Rayleigh-Bénard turbulence: Subregimes and their scaling relations for the Nusselt vs Rayleigh and Prandtl numbers. *Phys. Rev. Lett.* **133**, 144001 (2024).
24. J. J. Niemela, L. Skrbek, K. R. Sreenivasan, R. J. Donnelly, Turbulent convection at very high Rayleigh numbers. *Nature* **404**, 837–840 (2000).
25. J. J. Niemela, K. R. Sreenivasan, The use of cryogenic helium for classical turbulence: Promises and hurdles. *J. Low Temp. Phys.* **143**, 163–212 (2006).
26. P. Urban *et al*., Effect of boundary layers asymmetry on heat transfer efficiency in turbulent Rayleigh-Bénard convection at very high Rayleigh numbers. *Phys. Rev. Lett.* **109**, 154301 (2012).
27. K. P. Iyer, J. D. Scheel, J. Schumacher, K. R. Sreenivasan, Classical 1/3 scaling of convection holds up to $\mathrm{Ra} = 10^{15}$. *Proc. Natl. Acad. Sci. U.S.A.* **117**, 7594–7598 (2020).
28. M. K. Verma, P. K. Mishra, A. Pandey, S. Paul, Scalings of field correlations and heat transport in turbulent convection. *Phys. Rev. E* **85**, 016310 (2012).
29. A. Pandey, M. K. Verma, Scaling of large-scale quantities in Rayleigh-Bénard convection. *Phys. Fluids* **28**, 095105 (2016).
30. J. P. John, J. Schumacher, Strongly superadiabatic and stratified limits of compressible. *Phys. Rev. Fluids* **8**, 103505 (2023).
31. J. P. John, J. Schumacher, Compressible turbulent in highly stratified adiabatic background. *J. Fluid Mech.* **972**, R4 (2023).
32. H. Tiwari, L. Sharma, M. K. Verma, Compressible turbulent convection at very high Rayleigh numbers. *Int. J. Heat Mass Transf.* **242**, 126821 (2025).
33. D. Lohse, F. Toschi, Ultimate state of thermal convection. *Phys. Rev. Lett.* **90**, 034502 (2003).
34. P. Winchester, V. Dallas, P. D. Howell, Two-dimensional Rayleigh-Bénard convection without boundaries. *J. Fluid Mech.* **998**, A27 (2024).
35. S. Bhattacharya, M. K. Verma, R. Samtaney, Prandtl number dependence of the small-scale properties in turbulent Rayleigh-Bénard convection. *Phys. Rev. Fluids* **6**, 063501 (2021).
36. R. Samuel, M. K. Verma, Bolgiano-Obukhov scaling in two-dimensional Rayleigh-Bénard convection at extreme Rayleigh numbers. *Phys. Rev. Fluids* **9**, 023502 (2024).
37. R. Samuel, "Simulations of Rayleigh-Bénard convection at extreme Rayleigh numbers," PhD thesis (2023). https://www.researchgate.net/publication/391520596_PhD_Thesis.
38. E. A. Spiegel, Convective instability in a compressible atmosphere. *I. Astrophys. J.* **141**, 1068–1090 (1965).
39. E. Graham, Numerical simulation of two-dimensional compressible. *J. Fluid Mech.* **70**, 689–703 (1975).
40. A. G. Chatterjee *et al*., Scaling of a Fast Fourier Transform and a pseudo-spectral fluid solver up to 196608 cores. *J. Parallel Distrib. Comput.* **113**, 77–91 (2018).
41. U. Frisch, *Turbulence: The Legacy of A. N. Kolmogorov* (Cambridge University Press, Cambridge, 1995).
42. M. Lesieur, *Turbulence in Fluids* (Springer-Verlag, Dordrecht, 2008).
43. R. Samuel *et al*., SARAS: A general-purpose PDE solver for fluid dynamics. *J. Open Sour. Softw.* **6**, 2095 (2021).
44. P. Moin, W. R. Chan, *Fundamentals of Turbulent Flows* (Cambridge University Press, 2024).
45. G. Ahlers *et al*., Logarithmic temperature profiles in turbulent Rayleigh-Bénard convection. *Phys. Rev. Lett.* **109**, 114501 (2012).
46. H. Schlichting, K. Gersten, *Boundary-Layer Theory* (Springer, 2016).
47. S. B. Pope, *Turbulent Flows* (Cambridge University Press, Cambridge, 2000).
48. R. J. Samuel, M. Bode, J. D. Scheel, K. R. Sreenivasan, J. Schumacher, No sustained mean velocity in the boundary region of plane thermal convection. *J. Fluid Mech.* **996**, A49 (2024).
49. G. K. Batchelor, *The Theory of Homogeneous Turbulence* (Cambridge University Press, Cambridge, 1953).
50. D. C. Leslie, *Developments in the Theory of Turbulence* (Clarendon Press, Oxford, 1973).
51. A. Pandey, K. R. Sreenivasan, Transient and steady convection in two dimensions. *J. Fluid Mech.* **1015**, A42 (2025).
52. E. Lindborg, Scaling in two-dimensional Rayleigh-Bénard convection. arXiv [Preprint] (2025). http://arxiv.org/abs/2506.13213 (Accessed 29 July 2025).
53. V. Bouillaut, B. Flesselles, B. Miquel, S. Aumaître, B. Gallet, Velocity-informed upper bounds on the convective heat transport induced by internal heat sources and sinks. *Philos. Trans. R. Soc. A* **380**, 20210034 (2022).
54. S. Lepot, S. Aumaître, B. Gallet, Radiative heating achieves the ultimate regime of thermal convection. *Proc. Natl. Acad. Sci. U.S.A.* **115**, 8937–8941 (2018).
55. P. E. Roche, B. Castaing, B. Chabaud, B. Hebral, Observation of the 1/2 power law in Rayleigh-Bénard convection. *Phys. Rev. E* **63**, 045303(R) (2001).
56. S. Pirozzoli, M. Bernardini, R. Verzicco, P. Orlandi, Mixed convection in turbulent channels with unstable stratification. *J. Fluid Mech.* **821**, 482–516 (2017).
57. C. W. Hamman, P. Moin, "Numerical experiments in thermal convectionwith and without mean shear" (Tech. Rep. TF-170, Department of Mechanical Engineering, Stanford University, 2023).
58. R. Narasimha, K. R. Sreenivasan, Relaminarization of fluid flows. *Adv. Appl. Mech.* **19**, 221–309 (1979).
59. E. Calzavarini *et al*., Exponentially growing solutions in homogeneous Rayleigh-Bénard convection. *Phys. Rev. E* **73**, 035301 (2006).
60. G. Grötzbach, Spatial resolution requirements for direct numerical simulation of the Rayleigh-Bénard convection. *J. Comput. Phys.* **49**, 241–264 (1983).
61. Wesseling, *Principles of Computational Fluid Dynamics* (Springer-Verlag, Berlin Heidelberg, ed. 1, 2000).
62. C. Ouyang, S. He, Q. Xu, Y. Luo, W. Zhang, A MacCormack-TVD finite difference method to simulate the mass flow in mountainous terrain with variable computational domain. *Comput. Geosci.* **52**, 1–10 (2013).
63. S. Jagannathan, D. A. Donzis, Reynolds and Mach number scaling in solenoidally-forced compressible turbulence using high-resolution direct numerical simulations. *J. Fluid Mech.* **789**, 669–707 (2016).
64. H. Tiwari, L. Sharma, M. K. Verma, Repository for on the absence of the ultimate regime in turbulent thermal convection. [Zenodo] (2025). https://doi.org/10.5281/zenodo.16914627 (Accessed 20 August 2025).

Supporting Information for

On the Absence of the Ultimate Regime in Turbulent Thermal Convection

Harshit Tiwari, Lekha Sharma, and Mahendra K. Verma

Mahendra K. Verma
E-mail: mkviitk.ac.in

This PDF file includes:

Supporting Information Text

This section contains additional discussions on boundary layers, heat fluxes in two dimensions, and convergence tests, along with five figures and two tables. The table and figure captions are self-contained and provide the necessary context. This material acts only as a supplement to the main text.

Boundary layers in Turbulent Compressible Convection

In turbulent systems, boundary layers develop adjacent to the solid plates. The boundary layer profiles are often expressed in wall units: the friction velocity scale $u_\tau = \sqrt{\tau_w/\rho}$, wall temperature scale $T_\tau = -\kappa\, \partial_z \langle T\rangle_{A,t}|_{z=0}/u_\tau$, and length scale ν/u_τ, where $\tau_w = \mu\, \partial_z \langle u\rangle_{A,t}|_{z=0}$ is the wall shear stress, $\langle u\rangle_{x,t} = \langle\sqrt{u_x^2}\rangle_{x,t}$ in 2D, $\langle u\rangle_{A,t} = \langle\sqrt{u_x^2+u_y^2}\rangle_{A,t}$ in 3D, and ν and κ are the viscous and thermal diffusivities, respectively. In the above expressions, $\langle.\rangle_{x,t}$ and $\langle.\rangle_{A,t}$ denote the horizontal-time and planar-time averages (1–3). Using these variables, the nondimensionalized velocity, temperature, and vertical height z are $u^+ = \langle u\rangle_{A,t}/u_\tau$, $T^+ = (T_b - \langle T\rangle_{A,t})/T_\tau$, and $z^+ = u_\tau z/\nu$, respectively, where T_b is the temperature at the bottom plate.

According to the boundary layer theory (2, 3), there are two distinct regions:

$$\text{Viscous sublayer region } (z^+ < 5): \quad u^+ = z^+, \qquad T^+ = z^+, \tag{1}$$

$$\text{Log-law region } (z^+ > 50): \quad u^+ = \frac{1}{\kappa_u}\ln z^+ + B_u, \quad T^+ = \frac{1}{\kappa_T}\ln z^+ + B_T. \tag{2}$$

In these formulas, κ_u and κ_T are the von Kármán constants for the viscous and thermal boundary layers, respectively; and B_u and B_T are constants that depend on the flow configuration and boundary conditions. For pipe and channel flows, empirical and numerical studies reveal that κ_u varies from 0.39 to 0.41, and $B_u \approx 5.0$ for the viscous boundary layers (2, 4, 5). However, for the thermal boundary layers, κ_T and B_T often vary with the Prandtl and Reynolds number. Yaglom and Kader (6–8) argued that for Prandtl number near unity, κ_T ranges from 0.46 to 0.6 depending on the Reynolds number.

In the main text, we focused on the mean velocity and temperature profiles for compressible convection *near the bottom boundary*. In this Supplementary Material, we present the corresponding profiles *near the top wall*. The properties of the boundary layer near the top and bottom are similar, with minor differences, which are highlighted here. Figure S1(a,b) shows the mean velocity profiles $u^+(z^+)$ near the top boundary for both 2D and 3D simulations. For 2D compressible convection, the top plate exhibits a logarithmic layer, with κ_u decreasing from 0.96 at $\mathrm{Ra} = 10^9$ to 0.32 at $\mathrm{Ra} = 10^{16}$ (see Table S1). The above logarithmic layer is attributed to the shear flow present in the 2D flow. Note that κ_u for the top boundary is lower than that for the bottom boundary, indicating a stronger gradient and turbulence near the top boundary than the bottom boundary. In addition, the 3D velocity profile near the top boundary does not exhibit a clear logarithmic region, possibly due to the absence of a shear layer in 3D (9).

In Fig. S1(c,d), we plot the temperature profiles $T^+(z^+)$ near the top boundary. These plots exhibit a logarithmic layer in both 2D and 3D, similar to the bottom wall. The values of κ_T range from 4 to 12 for 2D and from 3.2 to 7.9 for 3D. Compared to the bottom boundary, on the whole, κ_T for the top boundary is larger for the 2D flows and smaller for the 3D flows. Also note that all four plots clearly show a viscous sublayer, with best-fit functions represented by black curves for $z^+ \lessapprox 2$. Lastly, Taylor-Couette flow and RBC have certain similarities, including in the boundary layers. However, these discussions are beyond the scope of this paper (10, 11).

Anisotropic Heat Fluxes in 2D Convection

We consider a snapshot of 2D periodic convection (PC) at Ra of 10^8, a snapshot of 2D RBC at Ra of 10^{14}, and a snapshot of 2D compressible convection (CC) at Ra of 10^{13} during the steady state, and display them in Fig. S2(a,b,c). The figure displays the vector plots of the velocity field $\mathbf{u}(\mathbf{r})$ and the density plots of the temperature field $[T(\mathbf{r}), T_{\rm sa}(\mathbf{r})]$, whereas Fig. S2(d,e,f) exhibits the vertical heat flux $F_z(\mathbf{r})$. As in 3D convection, periodic convection is dominated by positive F_z, but RBC and compressible convection have both positive and negative F_z's. However, compared to 3D convection, 2D convection exhibits stronger patches of positive and negative heat fluxes due to the inverse energy cascade in 2D (12, 13). These features are consistent with the wider tails in PDF's for F_z $[P(F_z)]$ in 2D than in 3D (see Fig. 5 of the main text).

Numerical Resolution and Convergence Tests

To ensure that our simulations at high Reynolds numbers are well-resolved, we performed detailed resolution and convergence tests. To accelerate convergence to a statistically steady state, for each case, we first conduct a simulation at a lower Ra, and then interpolate its final state onto a finer grid to initialize the subsequent higher-Ra run, repeating this procedure iteratively. For each run, we monitor the resolution parameter $\mathcal{R}_\eta = \min_i(\eta/\Delta x_i)$ and the number of grid points in the top and bottom boundary layers $(N_t^{\rm BL}, N_b^{\rm BL})$. Here, η is the Kolmogorov length; and Δx_i is the grid spacing in the i-th direction. We list these quantities in Table S2 (also see Table 1 of the main text). All our runs satisfy the resolution criteria, with $\mathcal{R}_\eta > 1$ for periodic convection and RBC, and $\mathcal{R}_\eta > 0.5$ for compressible convection (14, 15). Furthermore, the boundary layers are resolved with at least 7 grid points, thereby satisfying the Grötzbach criterion (16). The grid resolutions used in our simulations are comparable to those employed in previous high Reynolds number numerical studies (17, 18). For completeness and reproducibility, we also report in Table S2 a set of additional parameters: root-mean-square velocity U, normalized Nusselt number NuRa^{-b}, average time step $\langle\Delta t\rangle$, and the total simulation time $t_{\rm run}$ in free-fall units.

To test whether our simulations have reached a steady state, we plot the time series of root-mean-square velocity U and normalized Nusselt number NuRa^{-b} for the periodic and compressible convection for 10 free-fall times, where b is the exponent for Nu. For 3D and 2D periodic convection, after an initial transient, U (Fig. S3(a,c)) and NuRa^{-b} (Fig. S3(b,d)) are nearly constant, thus indicating convergence to statistical steady state. In periodic convection, the errors in U are below 17% while the errors in NuRa^{-b} are below 11%. The time series of 3D and 2D compressible convection exhibits similar behaviour (Fig. S4) with errors below 13% in U and below 20% in NuRa^{-b}. The total time of simulation t_{run} in 3D compressible runs is comparable to the past numerical study of 3D RBC by Iyer et al. (17). In compressible convection, we further verify grid independence at $\mathrm{Ra} = 10^{13}$ by comparing results on $501^2 \times 5001$ and $601^2 \times 6001$ grids (Fig. S5); both U and Nu converge to the nearly same value, independent of the grid resolution.

Regarding RBC, we refer the reader to Bhattacharya et al. (19) for details on the numerical resolution and convergence of the 3D RBC datasets, and to Samuel and Verma (20) and Samuel (21) for the corresponding 2D RBC datasets. It is well established in the literature that 3D RBC reaches statistical convergence more readily, with the root-mean-square velocity U converging in several free-fall times (17, 22). In contrast, for 2D RBC, Pandey et al. (13) and Lindborg (22) showed that the velocity field evolves more slowly than the thermal field, with the former converging exponentially slowly with time. Samuel and Verma (20) and Samuel (21) moved to higher resolution progressively, which leads to relatively faster convergence. Note, however, that the Nusselt number, which is the focus of this paper, exhibits relatively weaker fluctuations.

Table S1. For compressible convection C2D, C3D: Table exhibiting the von Kármán constants κ_u, κ_T for the viscous and thermal boundary layers near the top plate. It also lists the additive constants (B_u, B_T) near the top and bottom plates. Also see Table 1 of the manuscript.

System	Ra	Γ	$\kappa_{u,\mathrm{top}}$	$\kappa_{T,\mathrm{top}}$	$B_{u,\mathrm{top}}$	$B_{T,\mathrm{top}}$	$B_{u,\mathrm{bottom}}$	$B_{T,\mathrm{bottom}}$
C2D	10^9	1	0.96	4.1	6.2	0.25	2.7	−0.34
C2D	10^{10}	1	0.61	8.6	23	0.22	3.1	−0.63
C2D	10^{11}	1	0.48	8.5	14	0.31	2.7	−0.15
C2D	10^{12}	1	0.43	8	23	0.50	6.1	0.18
C2D	10^{13}	1	0.36	7.4	26	0.96	8.1	0.49
C2D	10^{14}	0.8	0.32	12	33	0.80	11	0.62
C2D	10^{15}	0.8	0.34	12	40	1.1	16	0.93
C2D	10^{16}	0.8	0.32	8	73	2.7	28	1.4
C3D	10^8	0.25	–	3.2	–	0.20	–	−0.07
C3D	10^9	0.25	–	3.6	–	0.22	–	−0.04
C3D	10^9	1	–	3.4	–	0.25	–	−0.11
C3D	10^{10}	0.25	–	4.6	–	0.37	–	0.04
C3D	10^{11}	0.25	–	5.7	–	0.41	–	0.07
C3D	10^{12}	0.125	–	5.1	–	0.53	–	0.09
C3D	10^{13}	0.125	–	7.9	–	0.60	–	0.15

Table S2. Additional parameters for periodic convection (P2D, P3D) and compressible convection (C2D, C3D): root-mean-square velocity U, normalized Nusselt number NuRa^{-b} (b = exponent for Nu), average time step $\langle \Delta t \rangle$, total time of the simulation t_{run} in free-fall time units, and the number of grid points in the top and bottom boundary layers (N_t^{BL}, N_b^{BL}).

Run	System	Ra	Pr	Grid Size	Γ	U	NuRa^{-b}	$\langle \Delta t \rangle$	t_{run}	N_t^{BL}	N_b^{BL}
1	P2D	10^4	1	64^2	1	1.5 ± 0.2	1.1 ± 0.1	1.0×10^{-2}	100	NA	NA
2	P2D	10^5	1	128^2	1	1.7 ± 0.1	1.1 ± 0.1	1.0×10^{-2}	100	NA	NA
3	P2D	10^6	1	256^2	1	1.7 ± 0.3	1.0 ± 0.1	1.0×10^{-2}	100	NA	NA
4	P2D	10^7	1	512^2	1	1.6 ± 0.2	0.9 ± 0.1	1.0×10^{-2}	100	NA	NA
5	P2D	10^8	1	1024^2	1	2.0 ± 0.1	1.0 ± 0.1	5.0×10^{-3}	100	NA	NA
6	P3D	10^4	1	128^3	1	1.8 ± 0.2	1.43 ± 0.07	1.0×10^{-2}	100	NA	NA
7	P3D	10^5	1	128^3	1	1.5 ± 0.1	1.24 ± 0.04	1.0×10^{-2}	100	NA	NA
8	P3D	10^6	1	180^3	1	1.5 ± 0.1	1.36 ± 0.06	1.0×10^{-2}	100	NA	NA
9	P3D	10^7	1	256^3	1	1.5 ± 0.1	1.46 ± 0.05	1.0×10^{-2}	100	NA	NA
10	C2D	10^9	0.7	513^2	1	0.34 ± 0.03	0.031 ± 0.004	7.5×10^{-4}	1150	32	11
11	C2D	10^{10}	0.7	1025^2	1	0.37 ± 0.02	0.030 ± 0.003	3.5×10^{-4}	1150	32	11
12	C2D	10^{11}	0.7	2049^2	1	0.37 ± 0.03	0.032 ± 0.005	1.2×10^{-4}	1150	30	10
13	C2D	10^{12}	0.7	4097^2	1	0.39 ± 0.03	0.036 ± 0.006	5.5×10^{-5}	400	31	10
14	C2D	10^{13}	0.7	8193^2	1	0.37 ± 0.03	0.034 ± 0.007	2.8×10^{-5}	100	34	10
15	C2D	10^{14}	0.7	12001^2	0.8	0.35 ± 0.02	0.029 ± 0.006	2.0×10^{-5}	72	28	9
16	C2D	10^{15}	0.7	16385^2	0.8	0.33 ± 0.02	0.036 ± 0.006	1.0×10^{-5}	27	25	8
17	C2D	10^{16}	0.7	24001^2	0.8	0.34 ± 0.02	0.029 ± 0.005	8.0×10^{-6}	19	23	7
18	C3D	10^7	0.7	$33^2 \times 129$	0.25	0.10 ± 0.02	0.037 ± 0.005	2.0×10^{-3}	1100	28	9
19	C3D	10^8	0.7	$65^2 \times 257$	0.25	0.13 ± 0.01	0.045 ± 0.004	2.0×10^{-3}	1100	32	12
20	C3D	10^9	0.7	$129^2 \times 513$	0.25	0.11 ± 0.01	0.046 ± 0.003	8.0×10^{-4}	200	31	11
21	C3D	10^9	0.7	513^3	1	0.16 ± 0.02	0.045 ± 0.001	8.0×10^{-4}	120	32	11
22	C3D	10^{10}	0.7	$257^2 \times 1025$	0.25	0.10 ± 0.01	0.044 ± 0.002	4.0×10^{-4}	250	30	10
23	C3D	10^{11}	0.7	$513^2 \times 2049$	0.25	0.10 ± 0.01	0.043 ± 0.001	2.0×10^{-4}	79	29	9
24	C3D	10^{12}	0.7	$451^2 \times 3601$	0.125	0.066 ± 0.002	0.039 ± 0.006	1.0×10^{-4}	26	23	8
25	C3D	10^{13}	0.7	$501^2 \times 5001$	0.125	0.064 ± 0.003	0.039 ± 0.005	8.0×10^{-5}	11	21	7

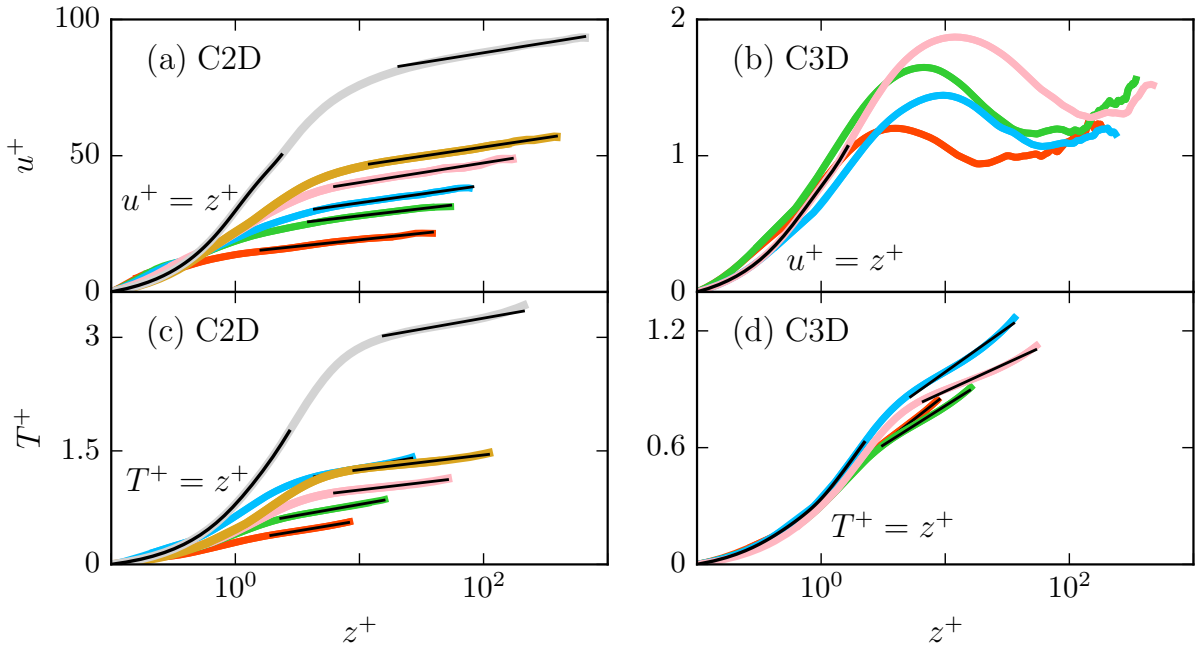

Fig. S1. Near the **top plate** of compressible convection, plots of u^+ vs. z^+ in the viscous boundary layers (top row: a,b), and T^+ vs. z^+ in the thermal boundary layers (bottom row: c,d). The left column is for 2D with Ra = 10^{11} (red), 10^{12} (green), 10^{13} (blue), 10^{14} (pink), 10^{15} (golden), and 10^{16} (gray). With increasing Ra, κ_u varies from 0.48 to 0.32, whereas κ_T varies from 8 to 11. The right column is for 3D with Ra = 10^{10} (red), 10^{11} (green), 10^{12} (blue), and 10^{13} (pink). Figure (b) does not exhibit a clear signature of the logarithmic layer. (d) For the thermal boundary layer in 3D, κ_T varies from 3.2 to 7.9.

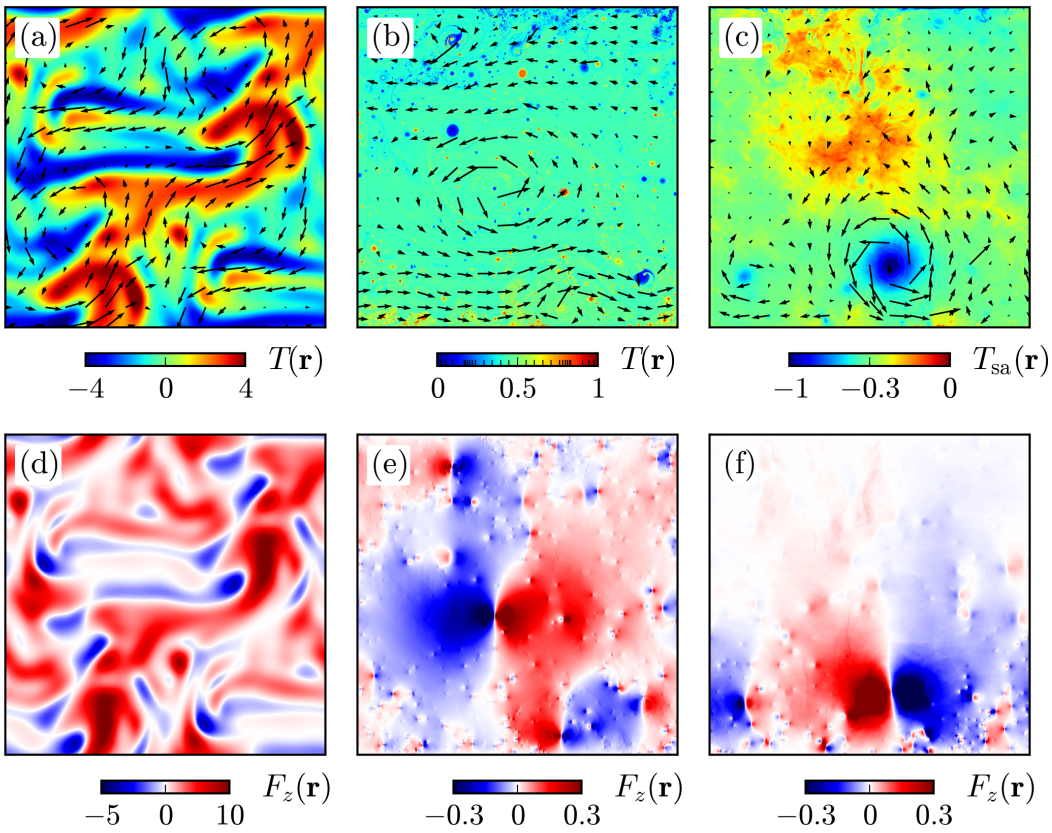

Fig. S2. For **2D convection**, plots of the velocity and temperature fields (top row), and vertical heat flux $F_z(\mathbf{r})$ (bottom row) for (a,d) 2D periodic convection with Ra = 10^8; (b,e) 2D RBC with Ra = 10^{14}; (c,f) 2D compressible convection with Ra = 10^{13}. Periodic convection exhibits predominantly positive F_z, whereas RBC and compressible convection exhibit both positive and negative F_z.

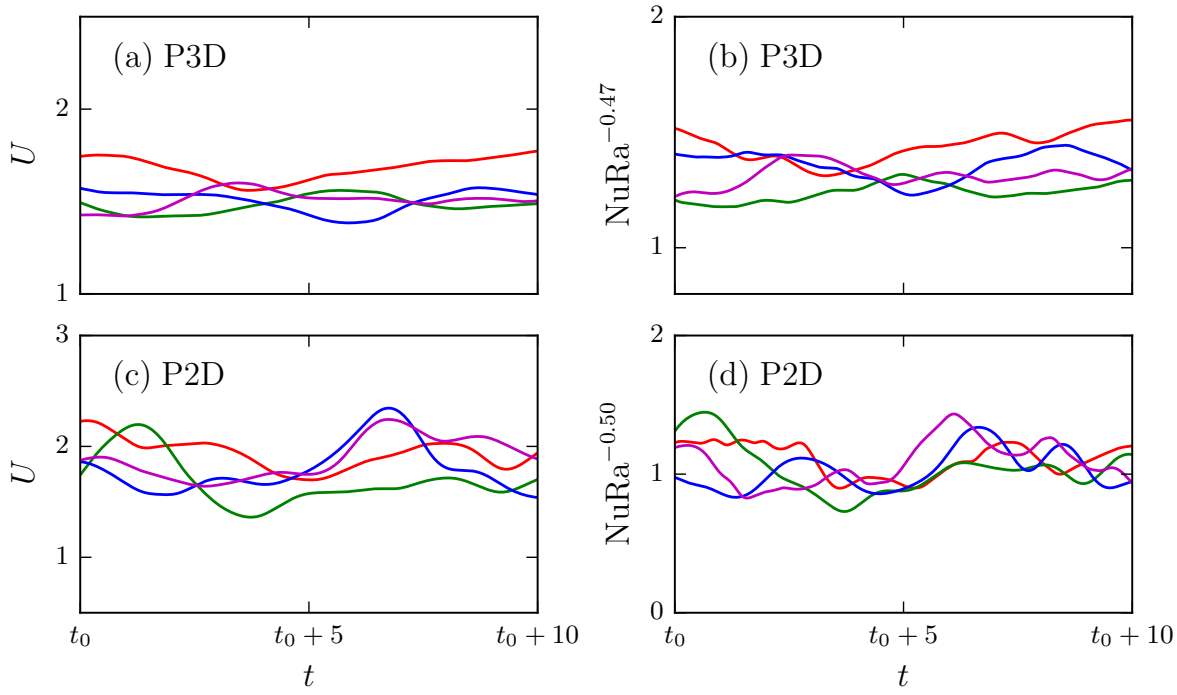

Fig. S3. For **periodic convection**, time series of the root-mean-square velocity U (a,c) and normalized Nusselt number NuRa^{-b} (b,d) during statistically steady state. The top row is for 3D at Ra $= 10^4$ (red), 10^5 (green), 10^6 (blue), and 10^7 (magenta). The bottom row is for 2D at Ra $= 10^5$ (red), 10^6 (green), 10^7 (blue), and 10^8 (magenta).

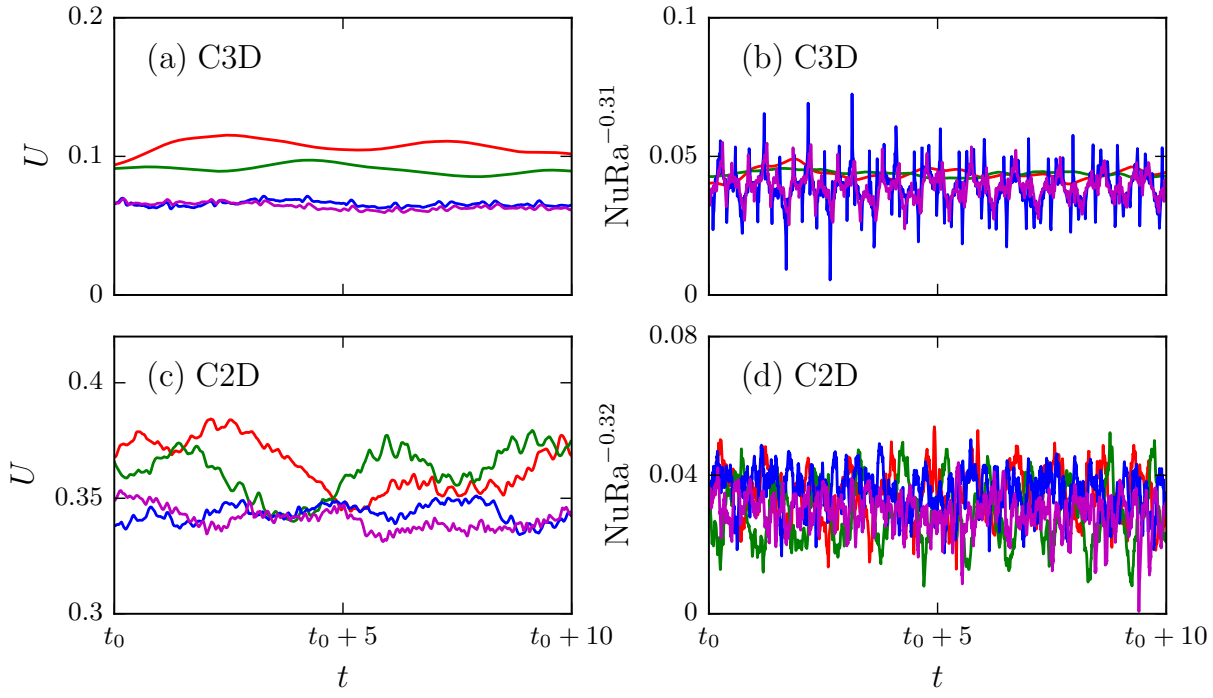

Fig. S4. For **compressible convection**, time series of the root-mean-square velocity U (a,c) and normalized Nusselt number NuRa^{-b} (b,d) during statistically steady state. The top row is for 3D at Ra $= 10^{10}$ (red), 10^{11} (green), 10^{12} (blue), and 10^{13} (magenta). The bottom row is for 2D at Ra $= 10^{13}$ (red), 10^{14} (green), 10^{15} (blue), and 10^{16} (magenta).

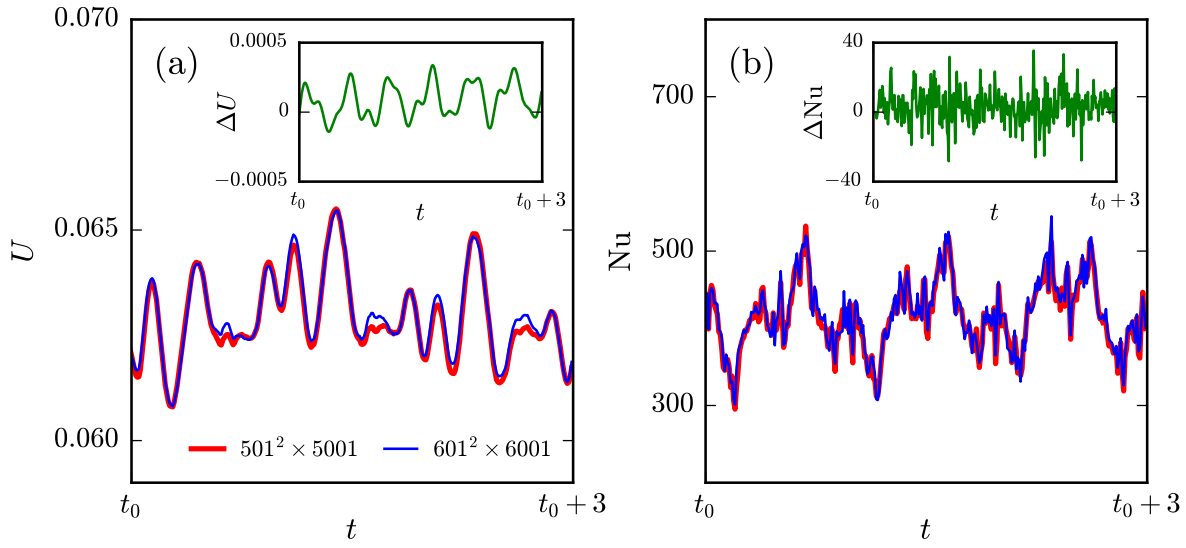

Fig. S5. For **3D compressible convection**, time series of the root-mean-square velocity U (a) and Nusselt number Nu (b) with Ra $= 10^{13}$ on grids $501^2 \times 5001$ (red) and $601^2 \times 6001$ (blue). Both U and Nu converge to similar values, confirming grid independence of our numerical simulations. The insets show their respective differences ΔU and $\Delta\mathrm{Nu}$ between the $601^2 \times 6001$ and $501^2 \times 5001$ grids. We took the final output of our $501^2 \times 5001$ grid resolution (highest 3D run), used it to perform two new simulations: on the same grid ($501^2 \times 5001$), and on the $601^2 \times 6001$ grid. We observed that the two runs yield similar results, but with some errors. The error in U is less than 1%, but the error in Nu is around 10%.

References

1. T Von Karman, Turbulence and skin friction. *J. Aero. Sci.* **1**, 1–20 (1934).
2. H Schlichting, K Gersten, *Boundary-layer theory.* (springer), (2016).
3. P Moin, WR Chan, *Fundamentals of Turbulent Flows.* (Cambridge University Press), (2024).
4. I Marusic, et al., Wall-bounded turbulent flows at high Reynolds numbers: Recent advances and key issues. *Phys. Fluids* **22**, 065103 (2010).
5. AJ Smits, BJ McKeon, I Marusic, High–Reynolds number wall turbulence. *Annu. Rev. Fluid Mech.* **43**, 353–375 (2011).
6. AM Yaglom, BA Kader, Heat and mass transfer between a rough wall and turbulent fluid flow at high Reynolds and Peclet numbers. *J. Fluid Mech.* **62**, 601–623 (1974).
7. AM Yaglom, Similarity laws for constant-pressure and pressure-gradient turbulent wall flows. *Ann. Rev. Fluid Mech.* **11**, 505–540 (1979).
8. BA Kader, Temperature and concentration profiles in fully turbulent boundary layers. *Int. J. Heat Mass Transf.* **24**, 1541–1544 (1981).
9. RJ Samuel, M Bode, JD Scheel, KR Sreenivasan, J Schumacher, No sustained mean velocity in the boundary region of plane thermal convection. *J. Fluid Mech.* **996**, A49 (2024).
10. FH Busse, The twins of turbulence research. *Physics* **5**, 4 (2012).
11. S Grossmann, D Lohse, C Sun, High-Reynolds Number Taylor-Couette Turbulence. *Annu. Rev. Fluid Mech.* **48**, 53–80 (2016).
12. EP van der Poel, RJAM Stevens, K Sugiyama, D Lohse, Flow states in two-dimensional Rayleigh-Bénard convection as a function of aspect-ratio and Rayleigh number. *Phys. Fluids* **24**, 085104 (2012).
13. A Pandey, KR Sreenivasan, Transient and steady convection in two dimensions. *J. Fluid Mech.* **1015**, A42 (2025).
14. S Jagannathan, DA Donzis, Reynolds and Mach number scaling in solenoidally-forced compressible turbulence using high-resolution direct numerical simulations. *J. Fluid Mech.* **789**, 669–707 (2016).
15. JP John, J Schumacher, Strongly superadiabatic and stratified limits of compressible convection. *Phys. Rev. Fluids* **8**, 103505 (2023).
16. G Grötzbach, Spatial resolution requirements for direct numerical simulation of the Rayleigh-Bénard convection. *J. Comput. Phys.* **49**, 241–264 (1983).
17. KP Iyer, JD Scheel, J Schumacher, KR Sreenivasan, Classical 1/3 scaling of convection holds up to Ra $= 10^{15}$. *Proc. Natl. Acad. Sci.* **117**, 7594–7598 (2020).
18. X Zhu, V Mathai, RJAM Stevens, R Verzicco, D Lohse, Transition to the Ultimate Regime in Two-Dimensional Rayleigh-Bénard Convection. *Phys. Rev. Lett.* **120**, 144502 (2018).
19. S Bhattacharya, MK Verma, R Samtaney, Prandtl number dependence of the small-scale properties in turbulent Rayleigh-Bénard convection. *Phys. Rev. Fluids* **6**, 063501 (2021).
20. R Samuel, MK Verma, Bolgiano-Obukhov scaling in two-dimensional Rayleigh-Bénard convection at extreme Rayleigh numbers. *Phys. Rev. Fluids* **9**, 023502 (2024).
21. R Samuel, Ph.D. thesis (2023).
22. E Lindborg, Scaling in two-dimensional Rayleigh-Bénard convection. *arXiv preprint arXiv:2506.13213* (2025).